

FERMIONIC STATE PREPARATION AND IMAGING IN OPTICAL TWEEZER ARRAY

Khoruzhii Kirill
Munich, May 29, 2025

Quantum simulation with ultracold atoms requires both high-fidelity preparation of the initial many-body state and site-resolved measurement of the final state. This thesis presents the development of experimental techniques for spin-resolved free-space imaging and deterministic, spin-selective preparation of ultracold fermionic ${}^6\text{Li}$ atoms in a two-dimensional optical tweezer array. The array is generated using crossed acousto-optic deflectors, with precise control achieved through a combination of direct camera-based calibration and atom-based feedback. A novel spilling method enables the preparation of arbitrary spin- and site-resolved occupation patterns. The thesis also introduces numerical tools for simulating Fermi-Hubbard dynamics in small systems, laying the groundwork for future out-of-equilibrium quantum simulation experiments.

Contents

1	Introduction	2
1.1	Quantum simulation with fermionic tweezer arrays	2
1.2	The Fermi-Hubbard model	2
1.3	Thesis outline	3
2	Experimental setup	4
3	Single-atom spin-resolved free-space imaging	6
3.1	Motivation and background	6
3.2	Experimental setup	7
3.3	Image processing	8
3.4	Spin-resolved detection	9
3.5	Spin manipulation	10
3.6	Conclusion	11
4	Tweezer array system	12
4.1	Motivation and concept	12
4.2	Optical setup	13
4.3	State preparation	14
4.4	Control	15
4.5	Tweezer depth balancing	16
4.6	Tweezer movement	17
4.7	Tweezer loading	18
4.8	Spin-selective spilling	19
4.9	Arbitrary occupation loading	20
5	Matter-wave magnifier	21
5.1	Motivation and overview	21
5.2	Numerical modeling	21
6	Fermi-Hubbard model: numerical approaches and simulations	24
6.1	Introduction	24
6.2	Dynamical phases	25
6.3	Numerical methods	28
6.4	Toolbox performance	29
6.5	Simulation example	29
7	Appendix	32
7.1	Boolean matrix factorization	32
7.2	Determinantal Point Processes	33

1 Introduction

1.1 Quantum simulation with fermionic tweezer arrays

The simulation of strongly correlated quantum systems remains one of the central challenges in modern physics. While exact numerical methods have provided deep insights in one-dimensional settings, the computational cost of simulating many-body dynamics in higher dimensions grows exponentially with system size, rendering classical approaches impractical. As first envisioned by Feynman, this motivates the development of physical quantum simulators that emulate target Hamiltonians using intrinsically quantum mechanical systems. Among several available platforms, ultracold atoms in optical potentials offer an exceptionally clean and versatile environment for realizing a broad range of many-body models, including the Fermi-Hubbard model relevant for high-temperature superconductivity [17, 19].

In particular, fermionic atoms loaded into optical lattices have enabled the realization of the two-dimensional Fermi-Hubbard model, with site-resolved imaging revealing spin correlations and signatures of antiferromagnetic ordering [35, 8]. These advances highlight the power of quantum gas microscopy in exploring equilibrium properties of lattice fermions. However, conventional approaches rely on thermal loading of large ensembles into periodic potentials, which often results in uncontrolled entropy and random filling defects. As a consequence, the system is typically initialized in a thermal ensemble, and the preparation of arbitrary low-entropy many-body states remains difficult.

Optical tweezer arrays offer an alternative, bottom-up approach. By providing single-site control, they allow deterministic preparation of initial states, flexible geometries, and site-selective addressing. While initially developed in the context of Rydberg atom arrays [10], these platforms have recently been extended to degenerate fermions, enabling programmable few-body Fermi-Hubbard dynamics [40, 44]. Such results position tweezer arrays as a promising architecture for scalable fermionic quantum simulators.

This thesis contributes to the development of a quantum simulation platform based on ultracold fermionic ${}^6\text{Li}$ atoms in a two-dimensional optical tweezer array. In this approach, the array is used for high-fidelity state preparation and control, while the optical lattice serves as the environment for Hamiltonian evolution. Compared to direct loading into a lattice, this separation of initialization and dynamics enables more efficient cooling, deterministic control over occupation patterns, and reduced cycle times. To support this workflow, we develop methods for spin-resolved free-space imaging, arbitrary pattern initialization via spin-selective spilling, and precise tweezer depth balancing.

Looking ahead, such a platform opens the door to nonequilibrium quantum dynamics. For instance, by performing randomized local operations followed by spin-resolved measurements, one can access entanglement entropy via measurement statistics [11]. These protocols offer a practical way to characterize entanglement growth and scrambling, even in regimes where full state tomography is infeasible. Extending such techniques to fermionic systems will provide new insights into thermalization, localization, and quantum information dynamics in strongly correlated matter.

In summary, this work supports the realization of a bottom-up fermionic quantum simulator by combining deterministic state preparation with single-atom, spin-resolved readout. These tools provide a foundation for studying both static and dynamical aspects of the Fermi-Hubbard model in a highly controlled setting.

1.2 The Fermi-Hubbard model

The Fermi-Hubbard model is a cornerstone theoretical framework for describing strongly correlated electron systems, particularly relevant in condensed matter physics for understanding the behavior of high-temperature superconductors, such as cuprates [28]. The Hamiltonian of the 2D Fermi-Hubbard model is typically expressed as:

$$H = -t \sum_{\langle i,j \rangle, \sigma} (c_{i,\sigma}^\dagger c_{j,\sigma} + \text{h.c.}) + U \sum_i n_{i,\uparrow} n_{i,\downarrow} + \sum_{i,\sigma} \varepsilon_i n_{i,\sigma}, \quad (1)$$

where the first term represents hopping with amplitude t between nearest-neighbor lattice sites, the second term describes the on-site interaction energy U , and the third term introduces site-dependent energy offsets ε_i , accounting for disorder or external potentials [28].

In physical terms, the competition between kinetic energy, captured by the hopping term, and potential energy, represented by the on-site interaction, gives rise to rich emergent phenomena. At half-filling and sufficiently large interaction strength $U \gg t$, the model predicts the formation of a Mott insulating phase, characterized by suppressed conductivity due to electron localization. At lower temperatures, antiferromagnetic correlations dominate, leading to spin ordering. Upon doping, the system can exhibit pseudogap behavior and potentially unconventional superconductivity analogous to that observed in cuprates, although achieving clear signatures of superconductivity in numerical and experimental studies remains challenging [28].

Beyond the single-layer scenario, the bilayer 2D Fermi-Hubbard model offers additional intriguing phenomena, including enhanced pairing mechanisms and novel magnetic orders. Experimentally realizing such bilayer systems could provide critical insights into mechanisms underlying high-temperature superconductivity. Within the UniRand

experiment, employing an accordion lattice geometry makes the exploration of bilayer configurations feasible, thereby opening new avenues for investigating these phenomena [26].

In the context of ultracold atoms, the Fermi-Hubbard model can be realized by trapping fermionic atoms, such as ${}^6\text{Li}$, in optical lattices, where parameters of the Hamiltonian can be precisely tuned. Specifically, the interaction parameter U is controlled via Feshbach resonances, where an external magnetic field is adjusted to tune the scattering length between atoms in different hyperfine states. This allows continuous tuning from attractive to strongly repulsive interactions, enabling experimental exploration of the full phase diagram [13].

The hopping amplitude t is controlled by adjusting the depth of the optical lattice potential. Deeper lattices decrease the tunneling rate, effectively increasing the ratio U/t and stabilizing strongly correlated insulating phases. Additionally, site-dependent potentials ε_i can be introduced via digital micromirror devices (DMD), allowing the controlled introduction of disorder or custom potential landscapes essential for exploring Anderson or many-body localization phenomena.

State preparation is envisioned to proceed via an initial deterministic loading of atoms into optical tweezer arrays, followed by a transfer into optical lattices. Such a procedure offers precise control over initial conditions, vital for exploring complex dynamical processes. Furthermore, measurement protocols incorporating Random Unitary Protocols, involving sequences of local random quenches and subsequent measurements, can yield critical information about the entanglement entropy and many-body coherence, significantly enriching experimental observables [13, 26].

1.3 Thesis outline

This thesis describes the development of experimental and computational tools for the preparation and probing of fermionic many-body states in a programmable optical tweezer array. The overarching goal is to enable bottom-up quantum simulation of lattice models, with precise control over initial conditions and single-atom, spin-resolved readout.

Sec. 3 presents the implementation of spin-resolved single-atom imaging of ${}^6\text{Li}$ in free space. The section describes the optical layout, the image processing pipeline, and introduces the Su-Schrieffer-Heeger model as a conceptual framework for understanding spin-dependent imaging dynamics.

Sec. 4 focuses on the creation and control of two-dimensional tweezer arrays. The section begins with the optical setup and AOD control, followed by a detailed discussion of calibration procedures and tweezer depth balancing using both camera-based and atom-based feedback. A key result is the development of a spin-selective spilling technique, enabling the preparation of spin- and site-resolved occupation patterns. Arbitrary configurations are realized through iterative removal steps, formalized via boolean matrix factorization.

Sec. 5 introduces the concept of a matter-wave magnifier—a lensing scheme designed to enhance spatial resolution for future lattice imaging. Although not yet implemented experimentally, fast simulations of wavefunction propagation and Monte Carlo sampling are presented to validate the scheme.

Finally, Sec. 6 outlines numerical approaches for simulating Fermi-Hubbard dynamics on small lattices. The computational framework combines exact diagonalization and Krylov-based time evolution, accelerated on GPU hardware. These tools enable simulations of dynamics in the presence of noise and disorder, and serve as a theoretical reference for upcoming experimental investigations.

2 Experimental setup

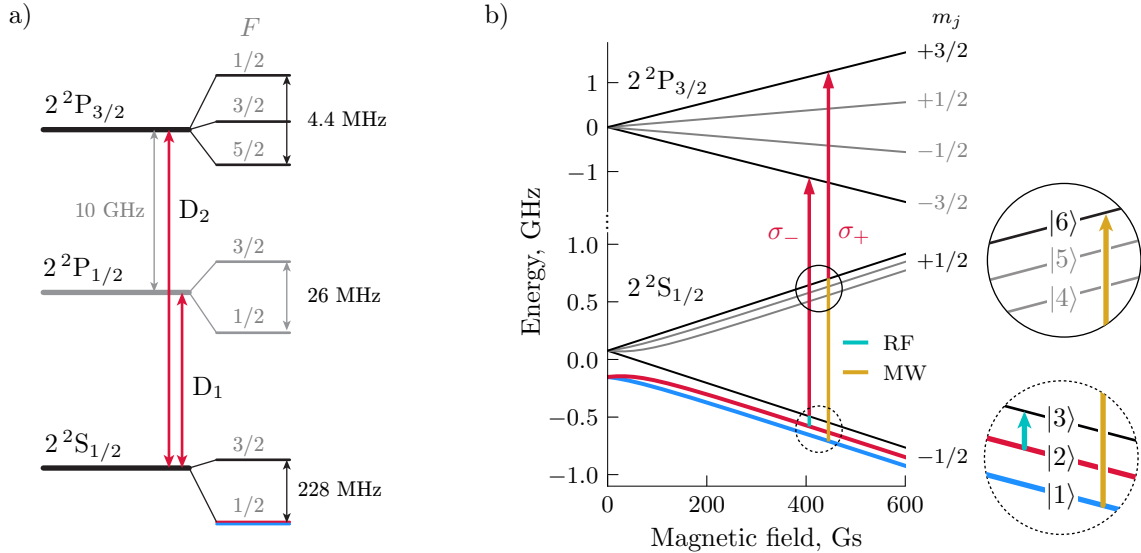


Figure 1: ${}^6\text{Li}$ energy levels. a) Level diagram of the ground and excited states of ${}^6\text{Li}$ [18], including the D₁ and D₂ transitions around $\lambda = 671$ nm. b) Zeeman splitting of the hyperfine levels of the $2^2\text{S}_{1/2}$ and $2^2\text{P}_{2/2}$ in ${}^6\text{Li}$ [39, 47]. As different spin states for physics we consider state $|1\rangle$ and $|2\rangle$, but for imaging it is worth to flip them to stretched states $|6\rangle$, $|3\rangle$. Colored lines indicate transitions driven by radiofrequency (RF) and microwave (MW) fields.

The UniRand experimental apparatus is designed to realize and investigate complex quantum many-body dynamics using ultracold fermionic ${}^6\text{Li}$ atoms. The primary objective of the setup is to create highly controllable initial quantum states, facilitate quantum simulation of the Fermi-Hubbard model, and enable precise measurements of quantum observables, such as entanglement entropy and particle correlations, by employing Random Unitary Protocols [13, 26].

The experimental procedure starts with ${}^6\text{Li}$ atoms emitted from an atomic oven. Lithium atoms are first collected and precooled in a two-dimensional magneto-optical trap (2D MOT), effectively capturing a high flux of atoms. From there, the atoms are transferred into a three-dimensional magneto-optical trap (3D MOT) for additional cooling and confinement, reaching temperatures near the Doppler limit (approximately $141 \mu\text{K}$ for ${}^6\text{Li}$) [13, 26].

Following the 3D MOT, atoms are loaded into a crossed optical dipole trap (ODT), generated by intersecting laser beams, creating a stable potential. At this stage, evaporative cooling further reduces the temperature significantly below quantum degeneracy conditions, reaching regimes where a molecular Bose-Einstein condensate (mBEC) can form. One of the first tasks within this thesis involved developing software for analyzing mBEC preparation data. Figure 2 illustrates results from this analysis, demonstrating the phase space density (PSD) increasing with reduced

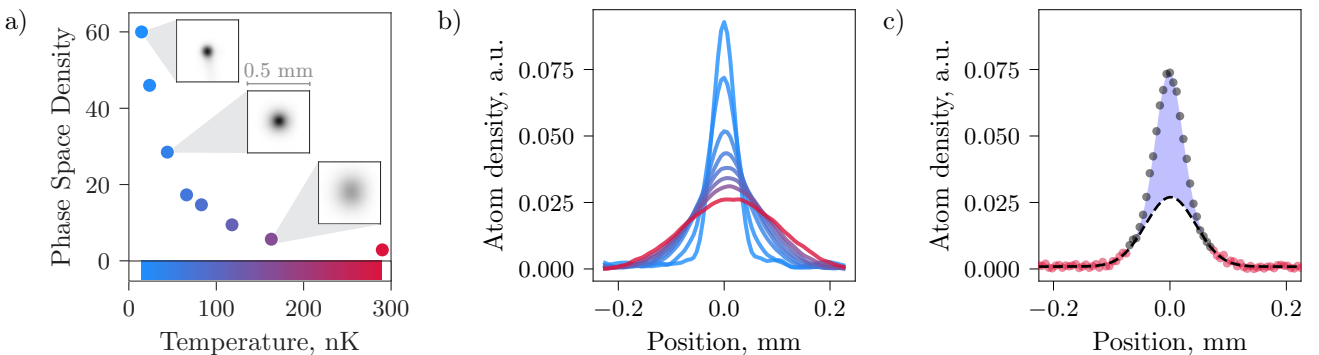


Figure 2: Molecular Bose-Einstein condensate data. (a) Phase space density (PSD) increases as temperature decreases via evaporative cooling, indicating condensation onset. (b) Atom density profiles normalized to unit area; color encodes temperature as in (a). (c) At low temperature, the profile shows a bimodal shape: a Gaussian fit to thermal wings (red dots) underestimates the central peak, revealing the mBEC component (blue area).

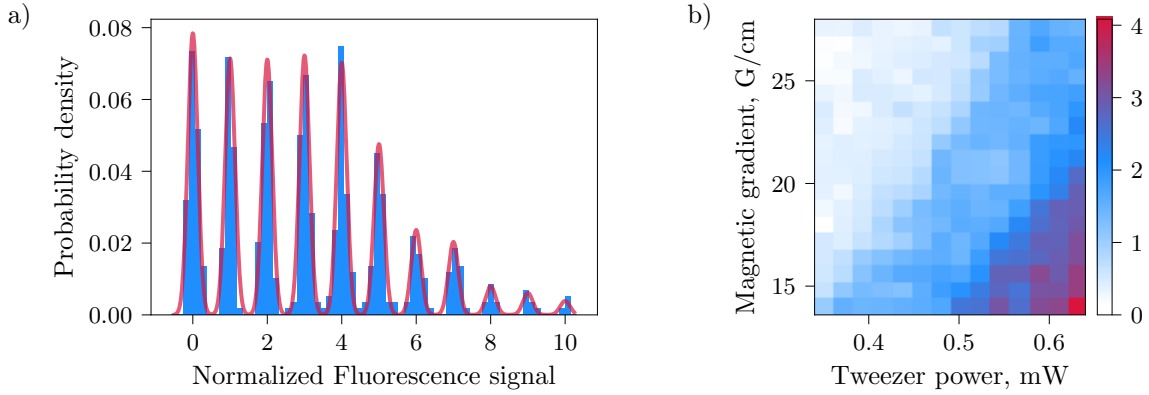


Figure 3: (a) Calibration histogram for single-atom counting based on fluorescence signal after loading to the MOT. Clear quantized peaks correspond to integer atom numbers; the solid red line is a multi-Gaussian fit to the distribution. (b) Measured 2D step plot as a function of tweezer power and magnetic field gradient. Each point indicates the average atom number obtained for a given combination of parameters. This map confirms that for any spill power, a suitable magnetic gradient can be found to achieve a desired quantized atom number.

temperature due to evaporative cooling (Fig.2a). Atom density profiles at various temperatures show a characteristic bimodal distribution at low temperatures, indicative of mBEC formation (Fig.2b). Fitting a Gaussian profile to the thermal wings of this distribution (red points in Fig.2c) clearly reveals a central peak representing the condensed fraction (blue shaded area in Fig.2c).

After reaching degeneracy in the ODT, atoms are adiabatically transferred into an optical tweezer array, typically implemented using crossed acousto-optic deflectors (AODs). These tweezers provide deterministic preparation of quantum states with single-site control. Precise atom number management is achieved through the spilling technique, which utilizes a magnetic field gradient and controlled reduction of tweezer depth to selectively retain atoms in low vibrational states [13, 26].

A critical aspect of our experiment is precise atom counting, particularly important when recapturing atoms from tweezers back into the MOT for calibration purposes. Atom number quantization can be clearly observed through fluorescence signal histograms, obtained with prolonged exposure times in a MOT loaded with a small number of atoms. Figure 3a shows discrete peaks corresponding to integer atom numbers, confirming accurate and reliable single-atom counting.

Future experimental plans involve transferring precisely prepared atoms into optical lattices engineered to simulate the Fermi-Hubbard model. Lattice depth and geometry, as well as disorder potentials, will be precisely tuned, with disorder introduced using a digital micromirror device (DMD), essential for studying localization phenomena [26].

High-resolution, spin-resolved imaging is crucial for detailed characterization of quantum states. Imaging employs fluorescence-based free-space techniques, enabling rapid and high-fidelity spin detection. Atoms are transferred to stretched hyperfine states, optimizing photon collection efficiency through closed cycling transitions.

Control over atomic spin states is executed using dedicated radiofrequency (RF) and microwave (MW) antennas. The PCB-based RF antenna drives MHz-range spin transitions, while the MW loop antenna efficiently couples to hyperfine transitions, enabling coherent manipulation critical for state preparation, spin-selective procedures, and precise quantum control.

The entire experimental cycle—including state preparation, evolution, and measurement—is optimized for rapid (cycle time is about 2s) and reliable repetition, allowing statistically robust data collection.

3 Single-atom spin-resolved free-space imaging

3.1 Motivation and background

Role of imaging in fast-cycle experiments. In high-repetition quantum simulation experiments with ${}^6\text{Li}$, fast, minimally disruptive, and high-fidelity single-atom detection is essential. Free-space imaging [6, 42] offers a simple and efficient alternative to traditional Raman-based fluorescence imaging. In this method, atoms are released from their traps and illuminated with resonant light. Fluorescence is collected without requiring additional cooling or deep pinning potentials. The short exposure time, typically around $10 \mu\text{s}$, allows for much higher experimental repetition rates compared to standard approaches based on quantum gas microscopes.

Free-space imaging for ${}^6\text{Li}$. Although ${}^6\text{Li}$ is a light atom and experiences relatively large momentum recoil during scattering, its broad D2 transition at $\lambda = 671 \text{ nm}$ allows for rapid photon emission. The typical recoil velocity is given by $v_{\text{rec}} = h/m\lambda$, where m is the atomic mass of ${}^6\text{Li}$ and λ is the wavelength of the imaging light. As the atom scatters photons at a rate Γ , each with random emission direction, it undergoes a random walk in momentum space. This results in spatial diffusion during the imaging pulse. The root-mean-square width of this random walk is approximately [30] (in the flashing regime)

$$\sigma_{\text{rw}} = \frac{1}{3} v_{\text{rec}} \Gamma^{1/2} t^{3/2}, \quad (2)$$

where t is the total exposure time. For a fixed number of scattered photons N_{ph} , we can express $t = N_{\text{ph}}/\Gamma$, yielding

$$\sigma_{\text{rw}} = \frac{1}{3} v_{\text{rec}} \Gamma^{-1} N_{\text{ph}}^{3/2}. \quad (3)$$

This scaling highlights the trade-off between collecting more fluorescence photons and maintaining spatial resolution. In our system, with $N_{\text{ph}} \sim 300$, the resulting diffusion is on the scale of $10 \mu\text{m}$.

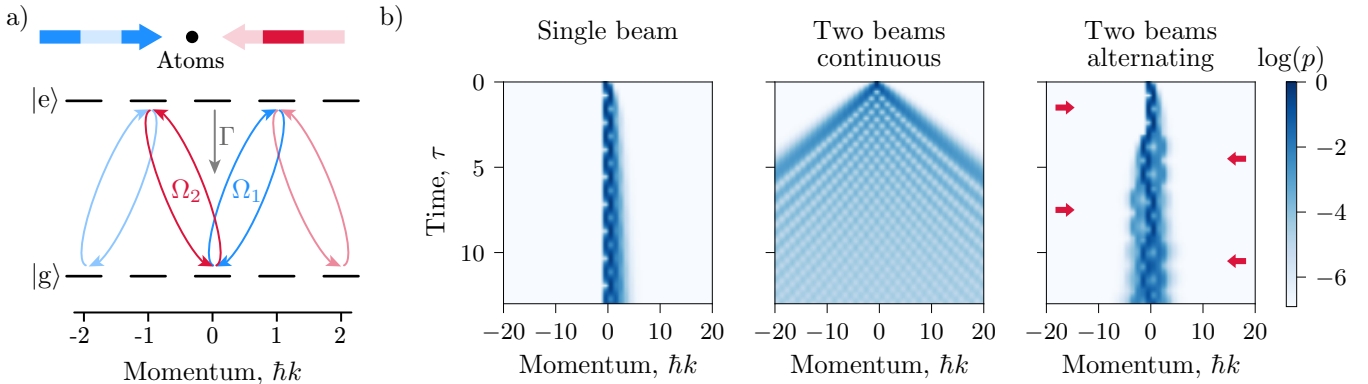


Figure 4: **Momentum-space dynamics in the SSH model.** a) Atoms undergo momentum-changing transitions via couplings Ω_1 and Ω_2 , realizing a SSH-like quantum walk. b) Momentum distributions over time for different beam configurations: single beam (left) shows small shift; two continuous beams (middle) result in fast spreading; alternating beams (right) suppress spread.

Connection to the SSH model. The scattering dynamics of a freely moving atom illuminated by resonant counter-propagating beams can be understood as a momentum-space quantum walk. This process maps onto the Su-Schrieffer-Heeger (SSH) model:

$$H = t_1 \sum_n |n, B\rangle \langle n, A| + t_2 \sum_n |n+1, A\rangle \langle n, B| + \text{h.c.}$$

In the atomic case, the model takes the form:

$$H = \frac{\Omega_1}{2} \sum_p |p, g\rangle \langle p+1, e| + \frac{\Omega_2}{2} \sum_p |p-1, e\rangle \langle p, g| + \text{h.c.}$$

Here, Ω_1 and Ω_2 correspond to the Rabi frequencies of the two beams. When both beams are on simultaneously, the atom undergoes coherent transitions between distant momentum states. This leads to rapid delocalization in space. The evolution can be simulated by solving a Lindblad master equation,

$$i\hbar \partial_t \rho = [H(t), \rho] + \mathcal{L}[\rho],$$

with \mathcal{L} describing spontaneous emission. These simulations show that applying the two beams alternately—rather than simultaneously—dramatically suppresses spatial diffusion and improves imaging fidelity (Fig. 4).

Spin-resolved imaging with stretched states. To perform spin-resolved detection with high signal strength,

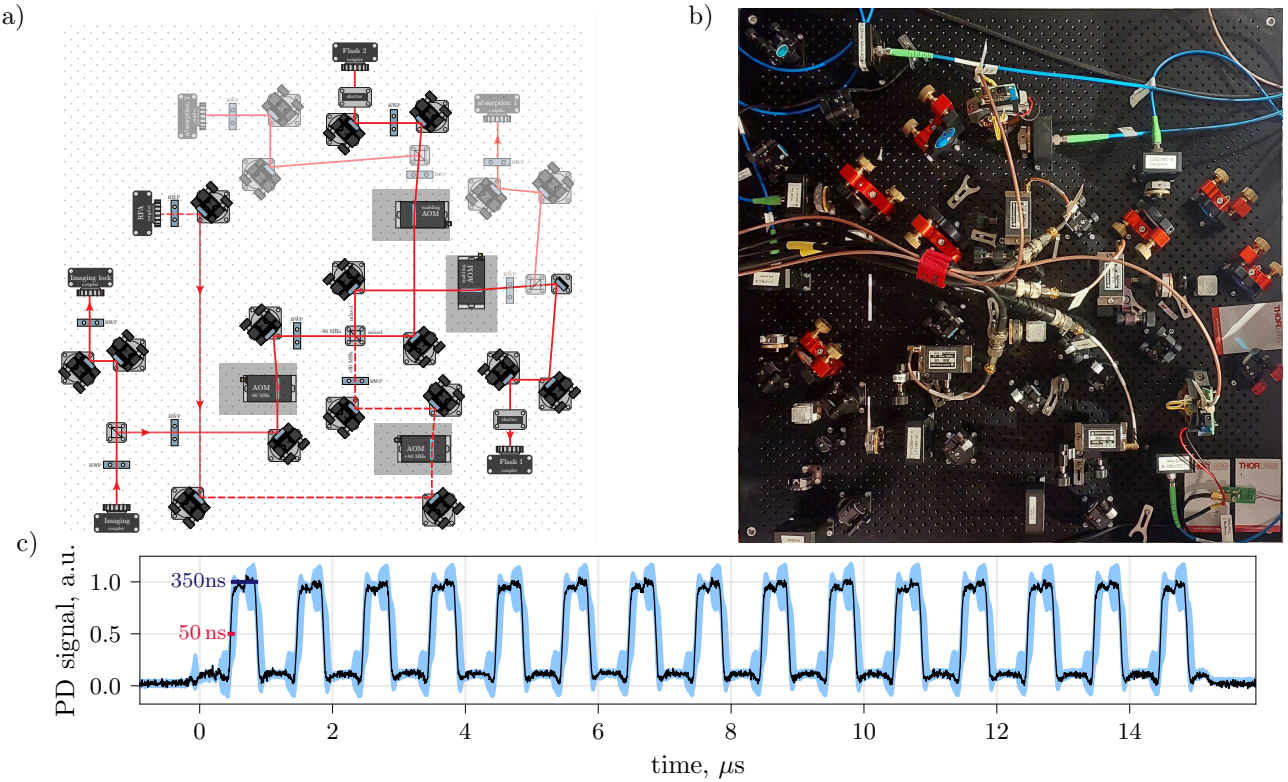


Figure 5: **Distribution board for flashing.** a) Optical layout of the board used to combine and control light for free-space imaging states $|3\rangle$ and $|6\rangle$. b) Experimental implementation. c) PD signal of the flashing measured on an oscilloscope (black – a single experimental run, blue – the standard deviation over 20 runs, red – rise time).

atoms are transferred into stretched states $|3\rangle$ and $|6\rangle$ before imaging. These states are nearly pure $m_J = \pm 1/2, m_I = \mp 1$ at high magnetic fields and couple strongly to σ^\pm polarized light. Unlike the commonly used $|1\rangle$ and $|2\rangle$ states, which have small admixtures that allow decay into dark states, $|3\rangle$ and $|6\rangle$ support nearly closed cycling transitions. As a result, atoms in these states scatter significantly more photons, often nearly twice as many, which greatly improves detection efficiency.

To distinguish the two spin states during a single imaging pulse, their respective fluorescence is spatially separated on the camera. This is achieved by using a polarizing beam splitter (PBS) after the objective, which directs σ^+ and σ^- components to different regions of the detector (see Fig. 7). By analyzing the relative photon counts in these regions, one can assign the spin state of each detected atom with high fidelity, as described in Sec. 3.4.

Overview of this section. The following subsections describe the complete implementation of spin-resolved free-space imaging in our experiment. Section 3.2 details the optical setup built and aligned during this work. Section 3.3 explains the image analysis pipeline, which was developed as part of this thesis. Finally, Section 3.4 presents the spin-state discrimination method and evaluates its fidelity using experimental calibration data. Together, these elements form a robust and fast readout protocol for our ${}^6\text{Li}$ tweezer-based simulator.

3.2 Experimental setup

Laser configuration and frequency scheme. The imaging system uses two frequency-stabilized diode lasers, each tuned to drive a stretched-state cycling transition in ${}^6\text{Li}$: $|3\rangle \rightarrow |3'\rangle$ and $|6\rangle \rightarrow |6'\rangle$. These transitions are addressed independently to enable spin-resolved fluorescence collection. Both lasers are frequency-locked to atomic references (see Appendix for further details on the stabilization scheme). The system does not require additional repumping during imaging, as both target states are closed under cycling.

Beam combination and modulation. The two lasers are routed through separate enabling AOMs (Gooch & Housego 3080-120, 120 MHz), which act as fast shutters. The output beams are then combined on a non-polarizing beam splitter (nPBS), producing two spatially overlapping but frequency-distinct outputs. This combination stage is duplicated to form two independent paths, which are later used to illuminate the atoms from opposite directions. Each combined beam is sent through a dedicated flashing AOM (Gooch & Housego 3080-120, 80 MHz), which controls the on-off modulation during imaging. The modulated light is then coupled into optical fibers, which deliver the light

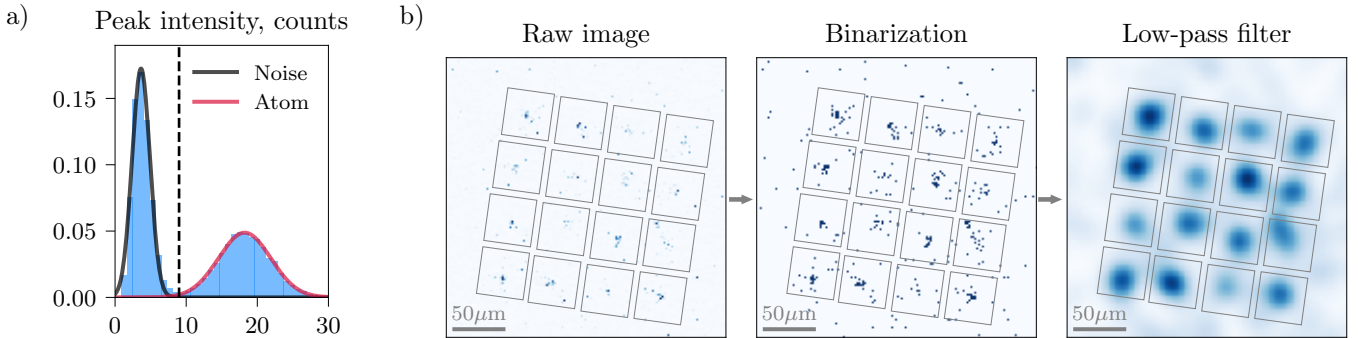


Figure 6: Single-atom identification and image processing. a) Histogram of peak intensities extracted from binarized and low-pass filtered images shows a bimodal distribution: the first peak corresponds to camera noise (black), the second corresponds to single atoms (red). The dashed line indicates the threshold used for atom identification. b) Image processing pipeline: Raw fluorescence image (left), binarization by intensity thresholding (center), and application of a low-pass filter (right) to reveal spatially localized atomic signals.

to the main experiment.

Flashing control and synchronization. To suppress recoil-induced diffusion (see Sec. 3.1), the two beams are pulsed in an alternating sequence. This is achieved by driving the flashing AOMs with square-wave TTL signals at 1 MHz, generated by a Rigol waveform generator. The generator itself is triggered by the experimental sequencer (ADwin), ensuring precise timing with respect to the overall shot cycle. Since the imaging beams operate well into the saturation regime, no active power stabilization is required during the imaging sequence.

Beam delivery and geometry. Both beams are collimated and directed onto the atom plane from opposite sides. No focusing optics are used; the beams are weakly converging and approximately collimated over the imaging region. Polarizations are adjusted to match the required σ^+ or σ^- conditions for selective excitation of $|3\rangle$ and $|6\rangle$. Fluorescence is collected through a high-numerical-aperture objective and split by a polarizing beam splitter (PBS), such that the σ^+ and σ^- channels are imaged onto separate regions of the camera. This layout enables single-shot spin resolution (see Fig. 7 and Sec. 3.4).

Implementation and contribution. The distribution board for imaging and RFA beams (including combining optics, AOM stages, and fiber coupling) was fully designed and assembled in the course of this work. This included optical alignment of the two combined beam paths and flashing channels. The downstream delivery system, from fiber coupler to atom plane, was implemented in collaboration with other team members. The beam alignment to atoms was carried out by the author, ensuring symmetric illumination and proper polarization for spin-selective excitation.

3.3 Image processing

Camera and detection regime. The imaging system uses a Nüvü HNü512 EMCCD camera, chosen for its high sensitivity and low noise in the few-photon regime. At $\lambda = 671$ nm, the sensor achieves a quantum efficiency (QE) of approximately 94% [30]. The camera is operated in photon counting mode with EM gain up to 5000, enabling single-atom detection from just tens of detected photons. During a typical imaging sequence, each atom emits around 300 photons, of which approximately 30 are detected on the camera after collection and transmission losses.

Binarization and filtering pipeline. To mitigate the excess noise factor (ENF) inherent in EM amplification and to suppress clock-induced charges (CICs), we apply a binarization scheme. A fixed threshold (typically $5\sigma_{\text{read}}$ above the baseline noise) is used to convert raw images into binary maps, where each pixel is marked as "bright" if it exceeds the threshold and "dark" otherwise. This removes ambiguity due to the stochastic gain distribution and allows images to be treated as photon arrival maps.

To reduce high-frequency noise while preserving localized atomic signals, we apply a Gaussian low-pass filter with a tunable width (typically $\sigma = 7$ px). This smooths the binarized images and helps identify spatially coherent clusters corresponding to single atoms. **Optionally, a denoising step based on a circular neighbor-count kernel can be applied after binarization; see Appendix for implementation details.**

Atom identification from local maxima. We locate candidate atom positions by searching for local maxima in the filtered images. Since the imaging beam is symmetric and atoms are spatially separated (due to the tweezer geometry), each atom forms a compact signal peak. To distinguish real atoms from CIC-induced noise clusters, we construct a histogram of peak amplitudes and apply a classification threshold based on the bimodal structure (see Fig. 6). This provides a robust method for single-atom detection within each image.

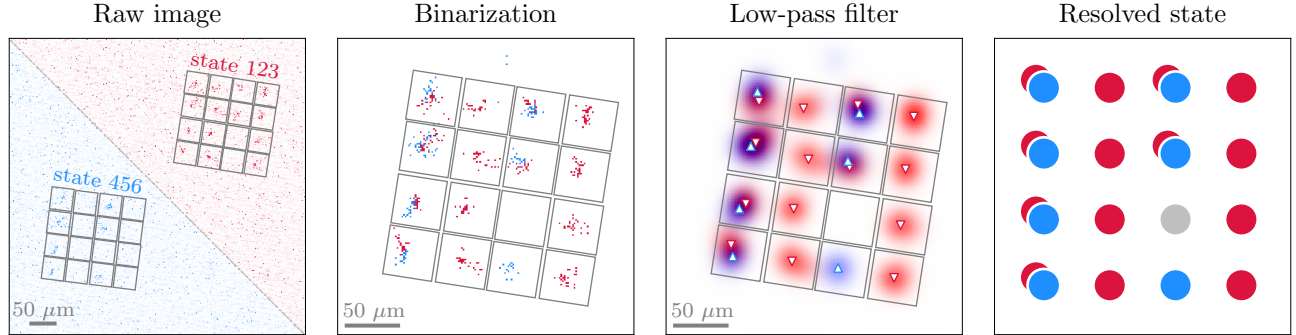


Figure 7: **Spin-resolved single-atom imaging.** Spatially separated σ_+ and σ_- fluorescence is imaged onto two distinct regions of the camera. The binarization step identifies photon counts above a threshold, followed by a low-pass filter to extract spatially localized signals. Final spin states are assigned based on relative signal strength in each channel: ● – $|1\rangle$, ● – $|2\rangle$, ● – no atom.

Use of ROI and regular array geometry. During this work, all experiments were performed with a regular tweezer array. This allows us to restrict image analysis to known regions of interest (ROIs) around each expected atom location. This prior knowledge significantly simplifies the classification problem: we identify the atom at a given site as present or absent based on the presence of a peak in the corresponding ROI. This enables more reliable classification than in fully general imaging tasks as in [6].

Implementation and contribution. The entire image analysis pipeline (bias correction, binarization, optional denoising, filtering, and classification) was implemented by the author in Python. The resulting code is vectorized and supports batch processing of image sequences. While the core concepts draw from existing methods developed in [6], the current implementation is adapted to the geometry and noise characteristics of our setup.

3.4 Spin-resolved detection

Single-shot spin resolution with spatial separation. Spin detection is implemented through a single-exposure fluorescence measurement, where the emitted light from atoms in $|3\rangle$ and $|6\rangle$ is directed to different regions of the camera. This spatial separation is achieved using a polarizing beam splitter (PBS) after the imaging objective, which splits σ^+ and σ^- components. In our geometry, atoms in state $|3\rangle$ produce fluorescence in the upper-right region of the frame, while those in $|6\rangle$ appear in the lower-left (see Fig. 7). The system is calibrated so that each site in the tweezer array corresponds to two fixed analysis regions—one per spin channel.

Filling detection. For each tweezer site, the signal is integrated within two predefined ROIs, each capturing the fluorescence from one spin channel. The presence and identity of an atom is determined by comparing the signals from the two channels. If the signal in only one ROI exceeds a detection threshold, the corresponding spin state ($|3\rangle$ or $|6\rangle$) is assigned. If neither region contains sufficient signal, the site is identified as empty. If both channels yield strong and spatially localized peaks, this is interpreted as the presence of two atoms in different spin states at the same site.

Fidelity estimation from single-atom preparation. To characterize the performance of spin-resolved detection, we use deterministic state preparation. In these experiments, each tweezer contains an atom with a known spin state ($|3\rangle$ or $|6\rangle$) with approximately 95% probability, as determined independently via fluorescence-based atom counting [16], see Fig. 3. Additionally, some chosen ROIs are intentionally left empty to provide ground truth data for evaluating false positive rates.

By applying the full detection pipeline to these experiments, we extract the rates of false positives (detecting an atom where none is present) and false negatives (failing to detect an atom where one exists). While the resulting classification accuracy depends on the overall filling fraction, the intrinsic detection characteristics (the false positive and false negative rates) are filling-independent. For a representative filling of 0.5, the resulting accuracy of spin-state assignment reaches 99%. This performance level is sufficient for the current experiment stage.

Implementation and contribution. The complete processing pipeline for extracting spin-resolved occupancy data from camera images was implemented by the author. The classification algorithm builds on the same architecture used for unpolarized imaging but includes support for analyzing two spatially distinct fluorescence regions per site. The code is vectorized for efficient processing and can be extended to support additional spin channels or dynamic configurations.

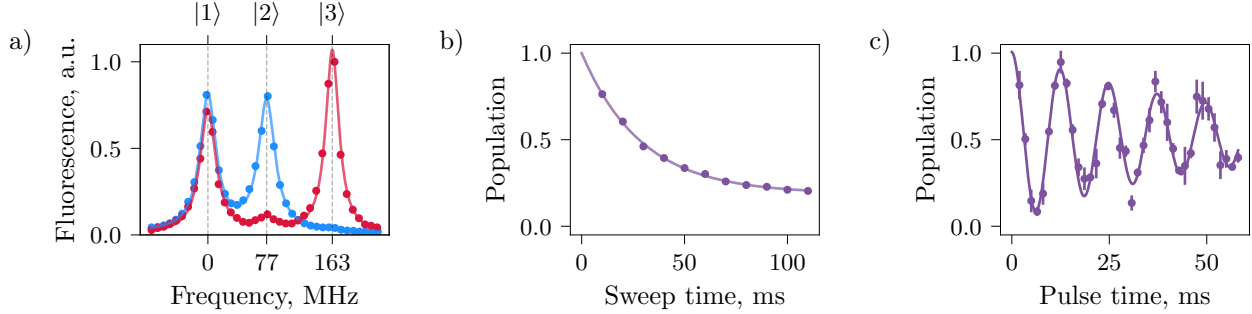


Figure 8: **Characterization of spin manipulation protocols.** (a) Fluorescence signal measured in the ODT before (blue) and after (red) applying a Landau-Zener sweep between states $|2\rangle$ and $|3\rangle$, showing population transfer to the target state. (b) Final population in $|2\rangle$ as a function of sweep duration, consistent with the Landau-Zener model. (c) Rabi oscillations observed when applying resonant RF π -pulse between states $|2\rangle$ and $|3\rangle$, demonstrating coherent control of the spin transition. (upd with 17.12.2024)

3.5 Spin manipulation

Introduction and motivation. Manipulating the internal spin state of ultracold atoms is an essential element in quantum simulation experiments, particularly for us in context of deterministic state preparation and spin-resolved imaging. Two widely employed methods for achieving controlled spin transitions in ultracold atomic systems are the Landau-Zener transition and coherent resonant π -pulse. The Landau-Zener approach involves adiabatically sweeping either the frequency of a driving field or the magnitude of a magnetic field across a spin-resonance. It has been widely applied due to its inherent robustness against small deviations in experimental parameters such as magnetic field fluctuations and frequency drifts. In contrast, the π -pulse method achieves spin flips by applying a resonant electromagnetic field pulse of precise duration, determined by the corresponding Rabi frequency. Although π -pulses offer considerably faster spin-flip operations, their fidelity is strongly sensitive to precise calibration of pulse duration, intensity, and frequency detuning, making them more susceptible to experimental noise and parameter instabilities.

Within the context of the current experiment, spin manipulation techniques serve two primary functions. Firstly, flipping atomic spins to stretched states enhances the efficiency of spin-resolved fluorescence imaging. Secondly, selective spin flips are integral to preparation protocols such as spin-selective spilling, allowing controlled removal of atoms in specific spin states. While the Landau-Zener method provided a practical starting point during initial setup stages (mainly due to its robustness against parameter variations) the progression toward faster experimental cycles motivated a transition towards using resonant π -pulses.

In the following paragraphs, the theoretical foundations of both Landau-Zener and π -pulse spin manipulation methods are described in detail. A comparative analysis then outlines their respective advantages and limitations in the presence of parameter noise, ultimately justifying the preferred choice adopted in this work.

Landau-Zener transition. The Landau-Zener (LZ) transition [32, 45] describes the non-adiabatic transition between two quantum states when the energy separation between these states is varied linearly in time. The Hamiltonian governing the dynamics of a two-level system undergoing such a process is expressed as:

$$H_{\text{LZ}}(t) = \frac{\hbar}{2} \begin{pmatrix} \Delta(t) & \Omega \\ \Omega & -\Delta(t) \end{pmatrix}, \quad (4)$$

where $\Delta(t)$ represents the instantaneous detuning between the system resonance and the external driving field, and Ω denotes the coupling strength (Rabi frequency) between the two states. Typically, the detuning is varied linearly as $\Delta(t) = \alpha t$, with α defined as the rate of change of detuning.

The transition probability P_{LZ} , derived analytically under the assumption of a linear sweep and constant coupling, is given by the Landau-Zener formula:

$$P_{\text{LZ}} = 1 - \exp \left(-\frac{\pi \Omega^2}{2\alpha} \right). \quad (5)$$

This probability explicitly depends on the ratio of the squared coupling strength Ω^2 to the detuning sweep rate α . For slow sweeps ($\alpha \ll \Omega^2$), the system achieves near-complete transitions ($P_{\text{LZ}} \rightarrow 1$), whereas faster sweeps reduce the fidelity (see Fig. 8b).

An important experimental advantage of the Landau-Zener method is its robustness against fluctuations in experimental parameters, such as variations in the magnetic field or the driving frequency. Small deviations in magnetic field gradients or frequency drifts typically have minimal impact on transition fidelity due to the exponential character

of Eq. (5). This robustness is particularly valuable in experiments where shot-to-shot variations in magnetic fields are inevitable.

Despite its robustness, the Landau-Zener transition requires relatively long timescales ($t_{LZ} \gg 1/\Omega$) to achieve high transition fidelities, which can slow down experimental cycles and increase exposure to decoherence processes.

Rabi π -pulse. An alternative technique for coherent spin manipulation is the resonant Rabi oscillation method, commonly known as the π -pulse approach. This method exploits coherent driving of the transition between two spin states at constant resonance, enabling deterministic and rapid population transfer.

The dynamics under resonant excitation are described by the Hamiltonian in Eq. (4) with a constant detuning $\Delta = \text{const}$. By applying a resonant driving field ($\Delta = 0$) for the duration $t_\pi = \pi/\Omega$, the system achieves complete inversion of the spin populations, thus realizing an ideal spin-flip operation between states $|1\rangle$ and $|2\rangle$.

The primary advantage of the π -pulse technique is its speed: the required pulse duration is significantly shorter than that for Landau-Zener sweeps ($t_\pi \ll t_{LZ}$), as evidenced by rapid Rabi oscillations in Fig. 8c. However, the fidelity of π -pulse transitions is highly sensitive to deviations from the exact resonance condition ($\delta \neq 0$), as well as inaccuracies in pulse duration and field amplitude. This sensitivity is captured analytically by the generalized Rabi oscillation formula:

$$P_\pi = \frac{\Omega^2}{\Omega^2 + \delta^2} \sin^2 \left(\frac{\sqrt{\Omega^2 + \delta^2}}{2} t_\pi \right). \quad (6)$$

Shot-to-shot fluctuations, especially those in the magnetic field, directly translate into variations in resonance conditions and consequently introduce systematic and random errors in spin-flip fidelity. As a result, consistently high fidelity using π -pulses necessitates stringent experimental stabilization of magnetic fields, pulse timing, and amplitude calibration.

In this experiment. In the present experiment, spin-state populations are routinely measured by scanning the laser frequency while simultaneously recording the fluorescence signal of atoms either confined in the ODT or directly in optical tweezers. Figure 8a demonstrates a typical example, showing clear fluorescence peaks corresponding to distinct spin states. Such spectral scans provide a reliable quantitative method for assessing the efficiency of spin-state transitions.

Initially, spin manipulation in this experiment relied primarily on Landau-Zener sweeps. Operating at moderate coupling strengths ($\Omega \sim 1$ kHz), transition fidelities around 95% were achieved. Subsequent technical improvements in the RF and MW antenna designs allowed increasing the effective coupling strength up to approximately 10 kHz. Employing π -pulses at this higher coupling strength consistently yielded fidelities of 99% or greater, primarily due to reduced sensitivity to decoherence over shorter timescales. In conclusion, while Landau-Zener sweeps provided a robust and convenient method for spin-state manipulation during initial setup phases, the improvements in RF/MW coupling strengths ultimately favored the adoption of faster and more efficient π -pulse protocols.

3.6 Conclusion

This chapter has detailed the implementation of a spin-resolved free-space imaging system for ${}^6\text{Li}$ atoms in an optical tweezer array. The approach is tailored to fast-cycle experiments and leverages the intrinsic spacing of the array to bypass the need for sub-micron spatial resolution.

The free-space fluorescence method was motivated both conceptually and practically, with an emphasis on momentum-space dynamics during imaging. Theoretical considerations based on the SSH model support the use of alternating beam sequences to reduce spatial diffusion, thereby improving localization fidelity.

The optical setup includes two independent laser beams driving stretched-state cycling transitions, with modulation handled via AOMs and synchronized control electronics. A distribution board was constructed to combine and route the beams, ensuring symmetric delivery to the atoms.

The image analysis pipeline applies binarization and spatial filtering to extract single-atom signals from low-flux data. The use of fixed array geometry enables simplified region-of-interest (ROI) analysis and improves classification reliability. All components of the processing chain are implemented in a parallelized, vectorized framework to support high-throughput acquisition.

Spin information is extracted by mapping fluorescence from σ^+ and σ^- transitions to distinct regions on the camera. A per-site classification algorithm assigns spin states based on signal strengths in these regions. Validation against calibrated single-atom counted experiments yields a classification accuracy of approximately 99% under typical experimental conditions.

These techniques constitute a fast and reliable imaging solution suitable for experiments requiring spin-resolved readout, and are readily extensible to future array sizes and imaging geometries.

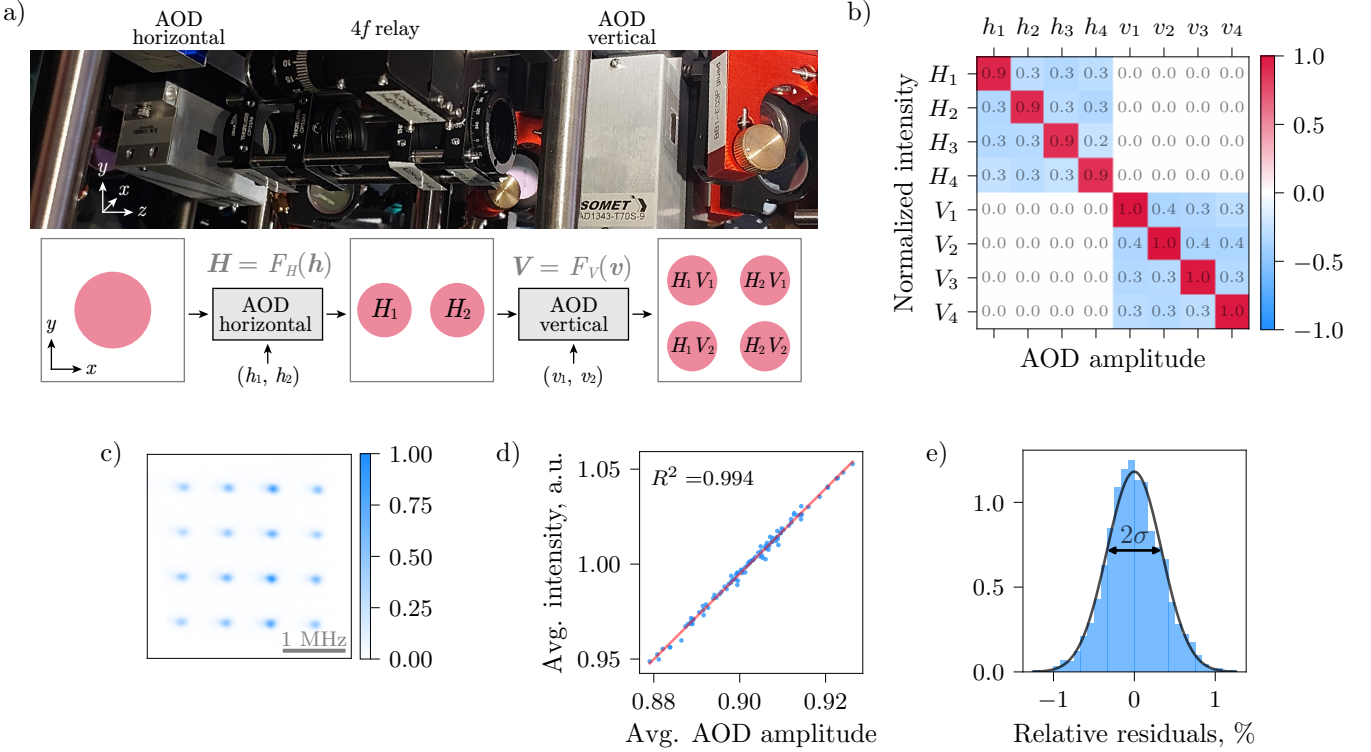


Figure 9: **Tweezer array control using orthogonal AODs.** (a) Experimental setup: two orthogonal AODs generate a 2D tweezer array. The applied harmonic amplitudes h_i, v_j define the output intensities $H_i = F_H(h)$ and $V_j = F_V(v)$ in horizontal and vertical directions, respectively. (b) Crosstalk matrix F' reconstructed via linear regression from camera images, showing how modulation of one harmonic affects others. (c) Example of measured intensity distribution at uniform input amplitudes ($h_i = v_j = 0.9$), illustrating imbalance in the resulting pattern. (d) The total intensity $\Lambda = \sum_{ij} H_i V_j$ scales linearly with the mean input amplitude. (e) Residuals of the linear model (fitted in the range $[0.85, 0.95]$) are normally distributed. All data were obtained in this work using direct camera-based measurements.

4 Tweezer array system

4.1 Motivation and concept

Optical tweezer arrays provide a flexible platform for preparing ultracold atomic systems with site-resolved control. By trapping individual atoms in focused laser beams, it becomes possible to initialize many-body states with controlled geometry, low entropy, and tunable local parameters.

In our setup, a two-dimensional array of tweezers is created using two orthogonal acousto-optic deflectors (AODs). Each AOD diffracts multiple beams along one axis, and their intersection forms the full array. The resulting intensity at site (i, j) factorizes as $P_{ij} = H_i V_j$, where H_i and V_j are set by the drive amplitudes applied to each AOD. This structure simplifies calibration and allows fast control of the entire array using a small number of parameters.

Compared to holographic or lattice-based approaches, the AOD system offers rapid reconfigurability and independent control of individual traps. This enables preparation of custom spin and density patterns, as well as dynamic manipulation during the experimental sequence. Such capabilities are useful, for example, for initializing specific configurations, removing defects, or performing spatially selective operations before loading atoms into an optical lattice for further evolution.

AOD operation. Each AOD consists of a crystal driven by a piezoelectric transducer. An incoming laser beam $(\mathbf{k}_{\text{in}}, \omega_{\text{in}})$ interacts with the induced acoustic wave (\mathbf{q}, Ω) via Bragg diffraction, producing an outgoing beam $(\mathbf{k}_{\text{out}}, \omega_{\text{out}})$:

$$\mathbf{k}_{\text{out}} = \mathbf{k}_{\text{in}} + \mathbf{q}, \quad \omega_{\text{out}} = \omega_{\text{in}} + \Omega.$$

The frequency Ω determines the deflection angle θ through the Bragg condition, while the amplitude of the RF signal controls the diffracted optical power. Each RF tone can be described by a triple $(\Omega_j, a_j, \varphi_j)$, corresponding to its frequency, amplitude, and phase. Applying a set of such tones to an AOD results in a superposition of multiple

diffracted beams, with the amplitude a_j determining the power in each beam and the phase φ_j influencing their relative coherence.

Factorized intensity distribution. To create 2D arrays, we combine two AODs oriented along orthogonal axes (fig. 9a), as described in [13]. Each axis is driven by a set of RF tones. In the paraxial approximation, the resulting 2D intensity pattern can be written as a rank-1 product of two vectors:

$$P_{ij} = H_i V_j,$$

where H_i and V_j correspond to the powers of individual beams generated by the horizontal and vertical AOD, respectively. The factorization of the output power can be verified via:

$$P \stackrel{\text{SVD}}{=} \sum_r \Lambda_r \mathbf{H}_r \mathbf{V}_r^T, \quad \text{factorisability} = \Lambda_0 / \sum_r \Lambda_r \quad (7)$$

which provides a natural measure of factorization. For arrays ranging from 2×2 to 10×10 , the factorisability measure $\Lambda_0 / \sum_r \Lambda_r$ is consistently above 0.99. For the 4×4 array used in most of our experiments, we obtain a typical value of 0.997(1).

Tweezer array control. The tweezer output beam powers are nonlinear functions of the input amplitudes \mathbf{a} :

$$P_j = F_j(\mathbf{a}) = F_j(\mathbf{0}) + F'_{ji} a_i + \frac{1}{2} F''_{j i_1 i_2} a_{i_1} a_{i_2} + \dots \quad (8)$$

The goal is to control¹ the full matrix P_{ij} using only two sets of parameters: horizontal amplitudes \mathbf{h} and vertical amplitudes \mathbf{v} .

It will later be necessary to reconstruct (H_i, V_j) from measured intensity distribution P_{ij} , so it is convenient to choose a factorized model $P_{ij} = \Lambda H_i V_j$, with the normalization:

$$\sum_i H_i = \sum_j V_j = 1, \quad \sum_{ij} P_{ij} = \Lambda.$$

This allows for an explicit decomposition:

$$\frac{1}{\Lambda} \sum_j P_{ij} = H_i \sum_j V_j = H_i, \quad \frac{1}{\Lambda} \sum_i P_{ij} = V_j \sum_i H_i = V_j, \quad \sum_{ij} P_{ij} = \Lambda, \quad (9)$$

which is fully equivalent to a rank-1 SVD of P_{ij} .

It is worth noting that, as shown in Fig. 9d, the total scale parameter Λ defined in this way is proportional to the total input amplitude, $a_{\text{sum}} = \sum_j h_j + \sum_i v_i$. This effectively decouples local balancing from global power constraints, simplifying the control problem.

4.2 Optical setup

Beam collimation and polarization. The tweezer array is formed by delivering light from a fiber outcoupler and collimating it with an $f = 40$ mm achromatic lens mounted on a translation stage for precise control. To ensure efficient diffraction through the acousto-optic deflectors (AODs), horizontal polarization is set using a $\lambda/2$ waveplate and a polarizing beam splitter (PBS). Correct alignment of the PBS is verified by tracking the beam position on a camera before and after insertion.

Acousto-optic deflectors and relay imaging. The array is generated using a pair of orthogonally mounted AODs, each mounted on custom blocks to maintain a common beam height of 100 mm. The beam is guided into the first AOD using two mirrors, and its alignment is optimized to maximize both transmission and diffraction efficiency (typically exceeding 90% at 65 MHz). The two AODs are connected via a 4f relay built from achromatic lenses in a 30 mm cage system. Precise positioning is achieved by aligning the relay externally using collimated light and checking for minimal wavefront distortion on a shear plate. An iris at the Fourier plane of the relay filters out the zeroth diffraction order.

Telescope and beam expansion. After the second AOD, the beam is expanded using a telescope consisting of $f = 150$ mm and $f = 500$ mm lenses. The alignment ensures that the beam is collimated and centered on both lenses. The position of the second lens is mechanically fixed, while the telescope length is adjusted via mirror positions to achieve good collimation, verified with a shear plate. The zeroth-order beam after the second AOD is blocked at the intermediate focus.

Monitoring and power balancing. A flip mirror is installed in the beam path to optionally redirect the light into a monitoring camera without disturbing the main optical alignment. This enables fast access to the tweezer array profile during alignment or balancing procedures.

We avoid using a back-side polished mirror for beam sampling in front of the camera. Although commonly employed for its simplicity, such mirrors introduce (? add measured data: october 2024) spatially varying interference fringes due to reflections from different internal surfaces of the substrate. These fringes distort the measured intensity distribution,

¹For amplitudes in the range $a_i \in [0.7, 1.0]$, we find that a linear or quadratic approximation suffices. In practice, we reconstruct the Jacobian matrix F'_{ji} using camera-based calibration, as discussed in Sec. 4.4.

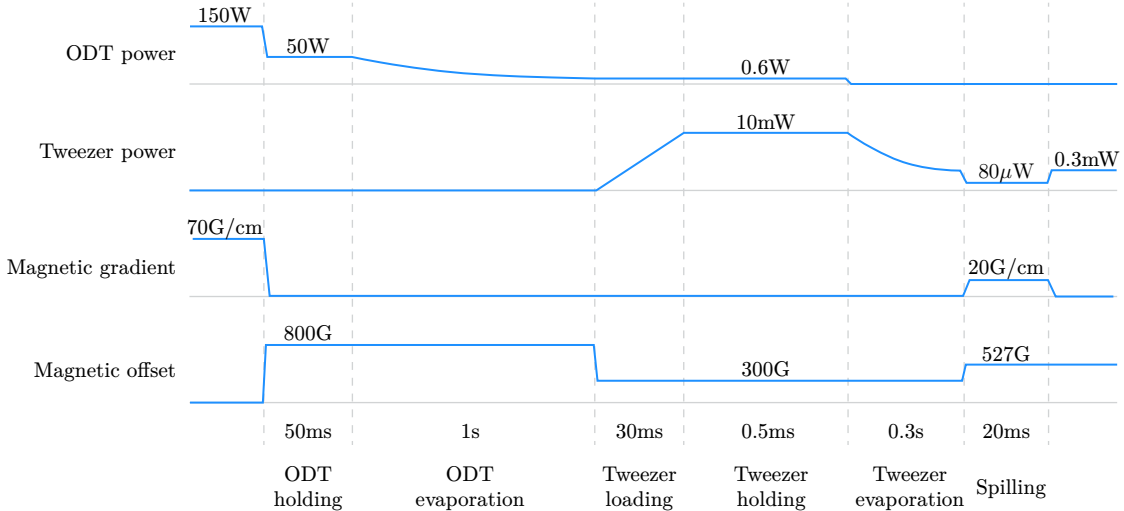


Figure 10: **Experimental sequence for deterministic atom number preparation.** After loading a spin-balanced mixture into a crossed ODT from the MOT, we perform two-stage evaporation in the ODT. The atoms are then transferred into an optical tweezer via an adiabatic ramp. Further evaporation is carried out in the tweezer before executing the spilling procedure. Spilling takes place at 527 G and a magnetic field gradient of 20 G/cm to remove atoms above the spill level. The full sequence enables high-fidelity few-body preparation within a sub-2 s cycle time. A detailed description can be found in [13].

especially for rays entering the camera at different angles and positions. This effect becomes critical when calibrating the response of the AODs, as it leads to systematic errors in measured beam uniformity. Instead, we sample the beam with a removable flip mirror that fully redirects the beam, ensuring an undistorted and angle-independent intensity profile at the camera plane.

4.3 State preparation

Tweezer loading. We begin by preparing a spin-balanced mixture in the two lowest hyperfine states, $|1\rangle$ and $|2\rangle$, using a compressed magneto-optical trap (MOT). The atoms are initially loaded into a crossed ODT, where we perform evaporative cooling. This follows closely the sequence described in [13].

After cooling, the atoms are transferred into a tightly focused optical tweezer potential. The loading process relies on the so-called *dimple trick* [46], where a tightly confined but deep tweezer potential is superimposed onto the wider ODT reservoir. Because the tweezer affects only a small region of the total cloud, the global temperature T remains approximately unchanged, while the local chemical potential is enhanced. In this regime, the average occupation

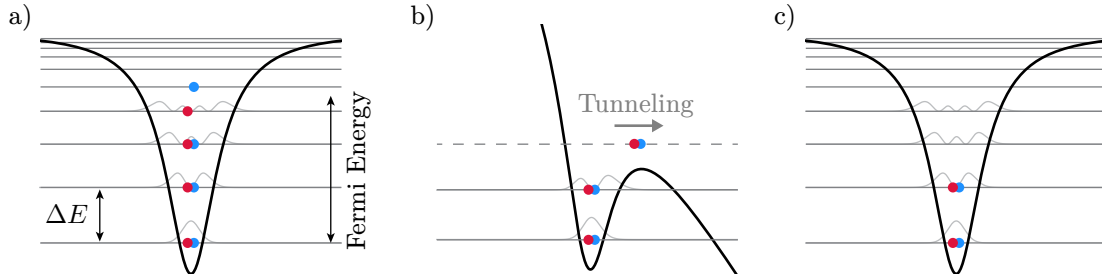


Figure 11: **Deterministic preparation via spilling.** (a) Fermionic atoms are initially loaded into a tightly confined optical tweezer, forming a Fermi sea occupying the approximately 1D harmonic oscillator levels up to the Fermi energy. (b) A magnetic field gradient tilts the potential, and the trap depth is lowered such that atoms above a defined spill level tunnel out. (c) This procedure leaves a well-defined number of atoms in the lowest energy states, with a preparation fidelity of approximately 95%. Blue and red dots denote atoms in different spin states; gray curves indicate the bound-state wavefunctions.

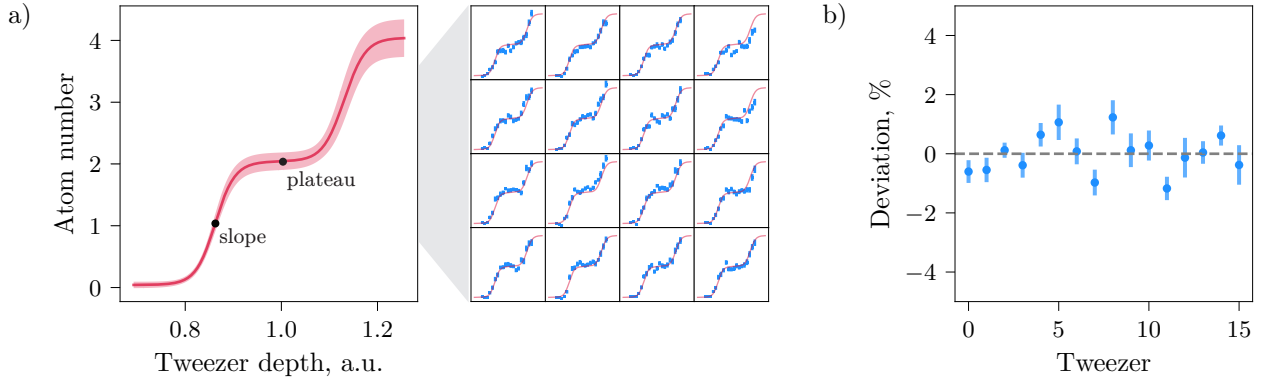


Figure 12: Step plot. (a) Atom number as a function of tweezer depth during the spilling sequence. Step plots for each tweezer in the 4×4 array are shown on the right. The average fit is shown as a solid red line, with standard deviation across sites indicated by the shaded area. (b) Relative deviation of the fitted sigmoid centers for each tweezer after SVF balancing. The standard deviation is $0.7(2)\%$, which is well within the plateau width ($\pm 5\%$), ensuring sufficient uniformity for array-wide spilling. χ^2 ?

number $\bar{n}(E_i)$ of a single-particle state i with energy E_i follows the Fermi-Dirac distribution:

$$\bar{n}(E_i) = \frac{1}{e^{(E_i - \mu)/k_B T} + 1}. \quad (10)$$

If the energy gap between the ground state E_0 and the Fermi energy E_F is increased such that $(E_0 - E_F)/k_B \gg T$, then $\bar{n}(E_0) \rightarrow 1$. This ensures near-unity occupation of the lowest level, which provides an ideal starting point for deterministic preparation. In our experiment, this condition is achieved by ramping on the tweezer adiabatically while continuing evaporation inside the tweezer. The full loading and cooling sequence is depicted in Fig. 10.

Deterministic few-body preparation via spilling. To isolate a well-defined number of atoms in the lowest motional states of the tweezer, we use the *spilling technique*, as described in [46, 23]. This method relies on tilting the potential with a magnetic field gradient and reducing the trap depth to allow atoms above a threshold energy to tunnel out. The resulting states are shown in Fig. 11. See Appendix for details.

The spilling sequence is performed at a magnetic field of 527 G, where the two spin states are nearly non-interacting. A magnetic field gradient of 20 G/cm creates a linear tilt, and the tweezer power is lowered to a value that sets the spill threshold. After a short tunneling time, the trap depth is ramped back up to recapture the remaining atoms. By empirically optimizing these parameters, we achieve deterministic preparation of two atoms per tweezer with a fidelity of approximately 95 %. This sequence results in high-fidelity preparation within a total experimental cycle time of less than 2 s.

4.4 Control

Frequency to position mapping. To extract the local intensities P_{ij} from camera images, we need to determine which pixels correspond to which tweezer sites. For this purpose, we define an affine transformation from the drive frequency space $(\omega_{\text{hor}}, \omega_{\text{ver}})$ to image plane coordinates (x, y) :

$$\mathbf{r} = H\boldsymbol{\omega}, \quad \Leftrightarrow \quad \begin{pmatrix} x \\ y \end{pmatrix} = \begin{pmatrix} h_{11} & h_{12} & h_{13} \\ h_{21} & h_{22} & h_{23} \end{pmatrix} \begin{pmatrix} \omega_{\text{hor}} \\ \omega_{\text{ver}} \\ 1 \end{pmatrix}.$$

Here, H is a 2×3 matrix calibrated from a set of measured spot positions. For example, one can measure \mathbf{r}_j for random frequency vectors $\boldsymbol{\omega}_j \in [\omega_{\min}, \omega_{\max}]$, construct the matrices ω_{ij} with $i \in \{\text{hor}, \text{ver}\}$ and r_{ij} with $i \in \{x, y\}$, and solve the least-squares problem:

$$\mathbf{r} = H\boldsymbol{\omega}, \quad \Rightarrow \quad \mathbf{r}\boldsymbol{\omega}^T = H\boldsymbol{\omega}\boldsymbol{\omega}^T \quad \Rightarrow \quad \mathbf{r}\boldsymbol{\omega}^T (\boldsymbol{\omega}\boldsymbol{\omega}^T)^{-1} = H. \quad (11)$$

This transformation defines a region of interest around each tweezer, within which we compute the integrated pixel intensity after background subtraction. The resulting values are proportional to the optical powers P_{ij} .

Linear reconstruction. The mapping from input amplitudes \mathbf{a} to optical power is approximated by Eq. (8). In the regime $a_i \in [0.85, 0.95]$, a linear approximation is sufficient². We construct the Jacobian matrix F'_{ji} by fitting a

²For wider amplitude ranges, higher-order terms can be added to the model. However, this is unnecessary in the present context.

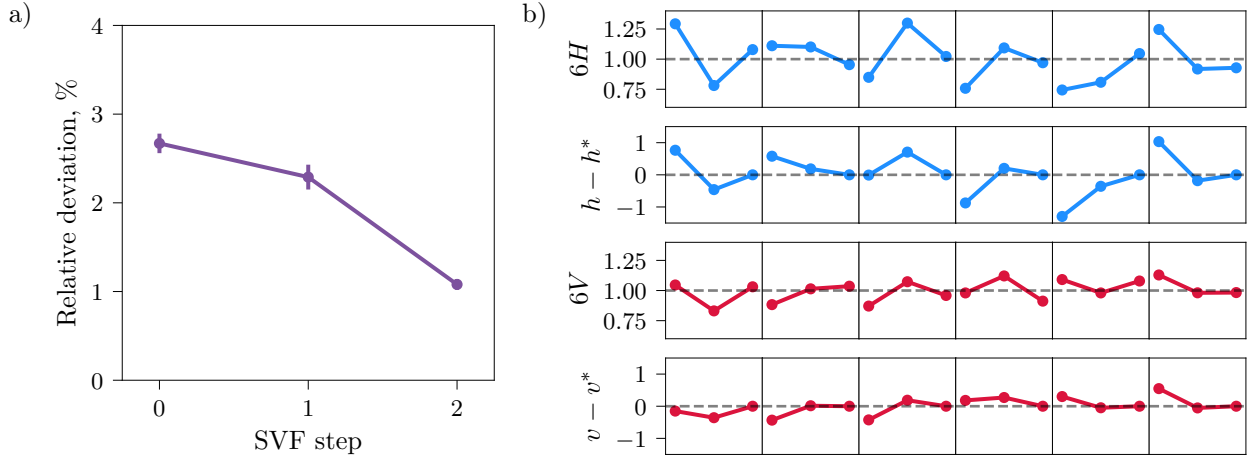


Figure 13: **Single-value feedback (SVF) optimization for a 6×6 tweezer array.** (a) Relative deviation of effective powers P_j across the array during successive SVF steps, quantified as $\text{std}(P_j)/\langle P_j \rangle$. The initial point corresponds to camera-based balancing; subsequent iterations apply SVF with feedback rates $\gamma = 1/20$ and $\gamma = 1/40$. Further iterations did not yield statistically significant improvements. (b) Retrieved horizontal powers H_i and vertical powers V_j (top and third rows), along with corresponding deviations of driving amplitudes from their final target values, $h - h^*$ and $v - v^*$. The recovered H , V vectors are extracted from the photon count matrix M_{ij} using factorization as described in (9).

linear regression model to a dataset of amplitude–intensity pairs. The resulting crosstalk matrix is shown in Fig. 9b. It is approximately diagonal, with comparable diagonal entries and off-diagonal elements typically reaching up to 30% in magnitude relative to the diagonal, due to power redistribution between neighboring tones. Crosstalk between the horizontal and vertical AODs remains negligible.

The quality of the linear fit for the 4×4 array is illustrated in Fig. 9e. The total intensity (Fig. 9d) scales linearly with the average input amplitude, yielding $R^2 > 0.99$. Relative residuals are normally distributed with width 0.3%, confirming the applicability of the model in this range.

Power-aware optimization. In the presence of limited laser power and finite AOM diffraction efficiency, we prefer solutions where all amplitudes remain close to 1. This preference can be incorporated into the optimization objective. In addition to minimizing intensity imbalance, we penalize deviations of the average amplitudes from a target value (e.g., 0.9).

4.5 Tweezer depth balancing

It is also possible to calibrate each AOD independently, without relying on an SVD-based approach. This alternative was not tested in the scope of this work. However, it is worth emphasizing that the SVD-based method is guaranteed to work even for double-AOD configurations [ref], where crosstalk between the two directions can be significantly stronger.

Precise control over the depth of each optical tweezer is essential for preparing few-fermion systems via spilling techniques. In our setup, each tweezer is initially loaded with approximately 100 atoms, which are then selectively removed by ramping down the potential depth. The number of remaining atoms as a function of spill power x_{sp} exhibits a quantized staircase structure, reflecting the discrete energy levels of the 1D harmonic oscillator. This behavior can be characterized by a step plot [23].

Step plot. To characterize this behavior in our tweezer array, we measure step plots for all sites simultaneously. Figure 12a shows the result for a 4×4 array. For each value of x_{sp} , we acquire 70 experimental realizations and compute the average photon signal per site.

Uniformity characterization. To quantify depth inhomogeneity across the array, we fit each step trace with a sigmoid function:

$$\text{sigmoid}(x) = \frac{A_j}{1 + \exp(-(x - x_j)/\sigma_j)},$$

where x_j denotes the center of the step and σ_j its width for tweezer j . We define a relative uniformity metric as $\text{std}(x_j)/\langle x_j \rangle$. After camera-based balancing (Sec. 4.4), this metric typically yields $\sim 3\%$, which is insufficient for deterministic preparation across the array. A more precise balancing procedure is therefore required.

Single-value feedback. To further improve uniformity, we apply an iterative atom-based feedback scheme. Rather than fitting full step plots, we operate at a single point on the slope of the transition, near the half-filling level $A_j/2$. At this point, the sigmoid can be approximated by a linear response:

$$\text{sigmoid}(x) \approx \frac{A_j}{4\sigma_j}x - \frac{A_j x_j}{4\sigma_j},$$

assuming $x_j \gg \sigma_j$. In the feedback loop, we do not use the fitted sigmoid parameters directly. Instead, we measure a single photon-count matrix M_{ij} and treat it as a linear proxy for the power matrix P_{ij} . Since the sigmoid offset shift = $A_j x_j / (4\sigma_j)$ is known from the fits, we approximate:

$$M_{ij} + \text{shift} \propto P_{ij} = \Lambda H_i V_j. \quad (12)$$

We then factorize this matrix using the method introduced in (9) and update the amplitudes according to:

$$h \rightarrow h + \gamma(H - H_0), \quad v \rightarrow v + \gamma(V - V_0),$$

where (H_0, V_0) is the target point, and γ is the feedback rate. This model-free procedure avoids full sigmoid fitting and operates directly on experimental measurements.

Figure 12b shows the result of applying this single-value feedback (SVF) protocol to a 4×4 array. After five iterations, the relative deviation of the fitted step centers is reduced to 0.7(2)% well within the plateau width (typically $\pm 5\%$), enabling deterministic state preparation across the full array. [Add fig. with single value feedback progress.](#)

Figure 13a shows the process of applying the SVF protocol to a 6×6 array. The proportionality coefficient in (12) is $A/4\sigma \sim 10(1)$ (the average value is chosen for the plot) for our experiment.

4.6 Tweezer movement

Tweezer movement. In experiments aiming at deterministic preparation and site-resolved imaging of individual ultracold atoms, precise and robust control over tweezer positions is crucial. In the present setup, while the Matter-Wave Magnifier (MWM) remains under development, single-atom imaging is achieved by initially positioning optical tweezers sufficiently far apart to individually resolve atoms. Specifically, atoms are loaded from the optical dipole trap (ODT) into tweezer potentials at an initial separation of $5\mu\text{m}$. Subsequently, this spacing is gradually increased to approximately $50\mu\text{m}$ by smoothly varying the driving frequencies of the acousto-optic deflectors (AODs), enabling direct optical resolution without additional magnification.

Transport trajectory optimization. The protocol chosen for tweezer translation critically influences the fidelity of atom transport. Naively, atoms can be moved by linearly ramping tweezer frequencies; however, such linear trajectories often lead to significant atom loss due to non-adiabatic excitations induced by abrupt changes in acceleration. To mitigate these losses, a smoother trajectory known as the Minimum-Jerk Trajectory (MJT) is employed. This trajectory is derived by minimizing the functional associated with the time-integrated square of the third derivative of the position, known as the jerk $j(t) = \ddot{x}(t)$:

$$\mathcal{J}[x(t)] = \int_0^T \left(\frac{d^3 x(t)}{dt^3} \right)^2 dt, \quad (13)$$

where $x(t)$ denotes the position and T the total transport duration. Minimization of Eq. (13), subject to the boundary conditions of initial and final positions $x(0) = x_i$, $x(T) = x_f$, and zero initial and final velocities and accelerations, yields a polynomial form:

$$x(t) = x_i + (x_f - x_i) \left[10 \left(\frac{t}{T} \right)^3 - 15 \left(\frac{t}{T} \right)^4 + 6 \left(\frac{t}{T} \right)^5 \right]. \quad (14)$$

This smooth polynomial interpolation minimizes abrupt changes in acceleration, thereby reducing non-adiabatic excitation and atom loss during transport.

To experimentally validate the efficacy of MJT compared to linear transport, systematic measurements were conducted. The fidelity of transport is defined as the probability of detecting an atom after transport, conditional upon its initial presence. As depicted in Fig. 14b, the MJT significantly outperforms the linear trajectory across a broad range of transport velocities. These measurements are obtained by initially holding atoms stationary for a fixed duration, thereby establishing a baseline population expected without transport-induced losses. Subsequently, atoms are transported along a zigzag path (forward and backward), and transport fidelity is measured relative to this baseline. Given the relatively low mass of ${}^6\text{Li}$ atoms, high transport velocities are achievable. Indeed, at typical experimental transport velocities of approximately $10\mu\text{m}/\text{ms}$, MJT achieves fidelities exceeding 99%, as demonstrated in Fig. 14b. This highlights MJT as the trajectory of choice for efficient and robust tweezer movement.

Detailed position versus time curves for both linear and MJT trajectories are shown in Fig. 14c. The MJT profile distinctly smooths acceleration and deceleration phases compared to the linear ramp, clearly illustrating the reduction in jerk. Correspondingly, experimental snapshots at various fractions of the total transport duration, depicted in

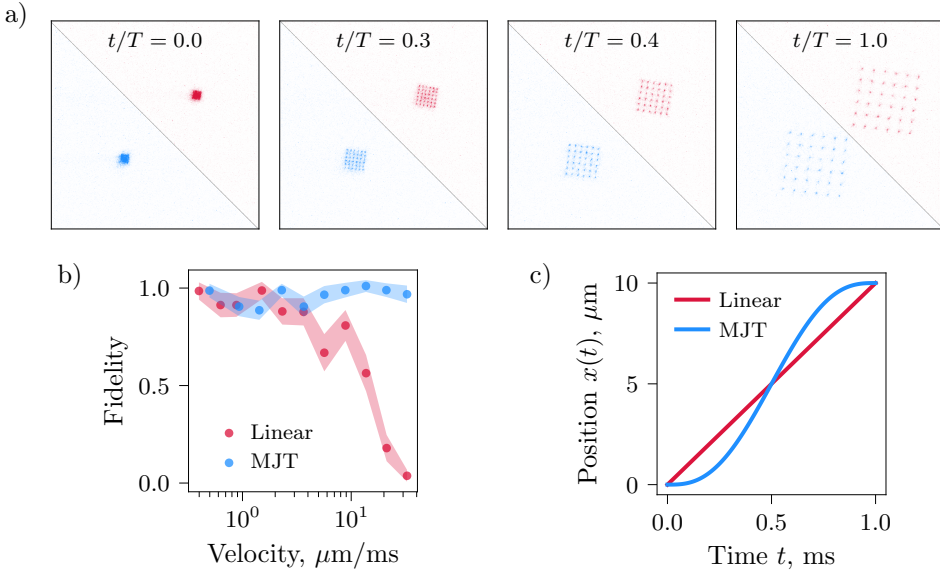


Figure 14: Characterization of tweezer transport protocols. (a) Snapshots at different fractions of the total transport duration, illustrating atom movement between initial and target tweezer positions during a typical experimental run. (b) Comparison of transport fidelity as a function of velocity for the Minimum-Jerk Trajectory (MJT) and linear trajectory. Fidelity is defined as the probability of detecting an atom after transport, conditional on its initial presence. (c) Position versus time curves for MJT and linear transport trajectories. Data points correspond to measurements, shaded areas represent standard deviation across realizations.

Fig.14a, visually confirm smooth and uniform atomic redistribution between initial and final positions. Each snapshot represents fluorescence images averaged over ten experimental realizations, confirming reproducible atom transport without significant losses or heating.

In summary, the implementation and systematic characterization of MJT for tweezer translation provides a critical improvement in transport fidelity compared to simple linear movements. The derived and experimentally validated MJT ensures minimal atom loss, thereby facilitating precise atom arrangement.

4.7 Tweezer loading

Even with meticulous balancing of tweezer intensities, residual imperfections inevitably persist in the final atom distributions. These imperfections arise from several distinct contributions, including tweezer movements, loading processes from the optical dipole trap (ODT), and fluorescence imaging. The present subsection specifically examines the influence of loading atoms from the ODT into the tweezer array, isolating this particular contribution from other experimental stages.

To systematically investigate loading effects, atom numbers in individual tweezers are measured directly after the **pre-evaporation** stage and prior to spilling. At this intermediate stage, the number of atoms per tweezer is inferred from the fluorescence signals recorded by the nuvu camera. Combining previously obtained calibration data from step plots and single-atom counting experiments (Sec. 3), approximately 30 photons per atom are expected to be detected by the camera, allowing quantitative estimation of atom populations per tweezer.

In the current setup, the minimum feasible spacing between tweezers is restricted to approximately $5 \mu\text{m}$. Attempts to further reduce this separation consistently resulted in elevated atom losses, presumably due to parametric heating effects associated with closely spaced potentials. Although stroboscopic methods—rapidly alternating between different AOD configurations—might mitigate these heating effects, such approaches require further systematic investigation and remain topics for future research. A dedicated characterization of minimal achievable spacing and associated atom retention rates is necessary and will be addressed in forthcoming studies (**add plot on the minimum distance between atoms in future**).

A preliminary investigation explored an alternative strategy: the dragging method, in which an array of tweezers is adiabatically translated through the ODT during loading. This approach allowed loading of larger tweezer arrays compared to the stationary loading method. However, despite its promise, the dragging method exhibited potential heating issues both in the ODT reservoir and within the tweezers themselves. The effectiveness of dragging critically depends on an accurate balance between tweezer and ODT depths, and careful optimization of these parameters also

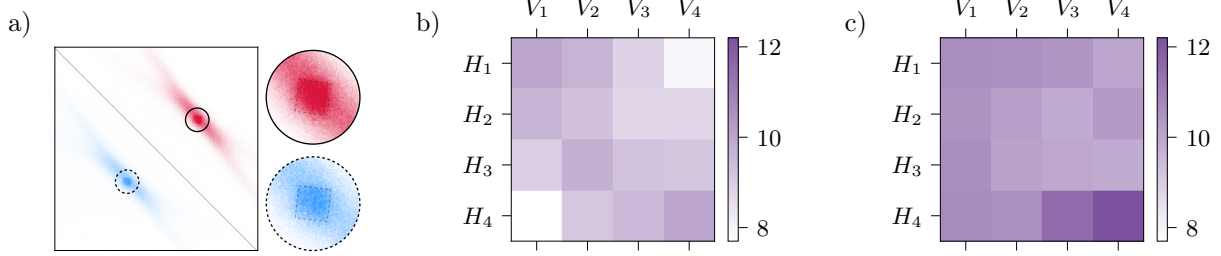


Figure 15: Inhomogeneous loading from ODT to tweezer arrays. (a) Atom distribution for a 6×6 array (averaged over 10 realizations), demonstrating inhomogeneous loading from the optical dipole trap (ODT). (b) Observed atom number distribution for a uniformly powered 4×4 tweezer array, revealing systematically lower loading efficiency at corners (averaged over 30 realizations). (c) Improved uniformity after manual adjustment of tweezer intensities, specifically enhancing corner powers (averaged over 30 realizations).

remains a necessary direction for future research.

With stationary loading at a fixed $5\text{ }\mu\text{m}$ spacing, systematic spatial inhomogeneities are consistently observed, particularly affecting the corner regions of the tweezer array. This effect is illustrated clearly in Fig. 15a, which shows an averaged atom distribution for a 6×6 tweezer array directly after loading from the ODT. Atom occupancy at corner sites is markedly reduced relative to central sites. A quantitative assessment of loading imbalance is provided in Fig. 15b, depicting the measured atom number distribution for a uniformly powered 4×4 tweezer array. The corners show systematically lower populations compared to central positions.

To overcome this intrinsic loading imbalance, a manual redistribution of tweezer intensities was performed using the previously measured camera-based crosstalk matrix. Specifically, the intensities of corner tweezers were deliberately increased relative to central tweezers to compensate for the lower initial loading rates. This simple yet effective manual intervention improved corner loading significantly, increasing atom numbers at corner positions by approximately 20% as demonstrated in Fig. 15c. Consequently, this intensity adjustment facilitated more homogeneous atom distribution and higher fidelity in subsequent state preparation procedures.

In summary, careful analysis and targeted intensity adjustments during the ODT loading phase substantially reduce residual inhomogeneities in atom occupancy. However, further improvements and more systematic methods—including minimal spacing optimization, stroboscopic techniques, and dragging approaches—represent valuable areas for continued research.

4.8 Spin-selective spilling

After balancing the tweezer depths and performing standard spilling to prepare unit filling (one atom in state $|1\rangle$ and one in $|2\rangle$ per site), atoms in a selected spin state can be selectively removed while leaving the other unaffected. This enables the preparation of arbitrary spin-resolved configurations, a crucial ingredient for bottom-up simulation of spinful many-body systems.

Magnetic-field dependence. The key idea relies on the difference in magnetic moments between the hyperfine ground states. As shown in Fig. 1b, the energy of state $|2\rangle$ exhibits a maximum near 27 G, where its magnetic moment vanishes: $\mu_{|2\rangle} = \partial E / \partial B = 0$. In contrast, state $|1\rangle$ has a sizable negative magnetic moment at this field (**write down value**). As a result, when a magnetic field gradient is applied at $B = 27$ G, only atoms in state $|1\rangle$ experience a significant force and are spilled from the traps.

Spin-selective removal. The experiment starts with a $|1\rangle - |2\rangle$ spin mixture at unit filling in each tweezer. The magnetic field is ramped to 27 G, and a field gradient is applied. This results in spin-selective spilling: atoms in state $|1\rangle$ are removed, while those in $|2\rangle$ remain confined.

The crossed AOD configuration enables control over the local optical power P_{ij} through factorized amplitudes, such that $P_{ij} = H_i V_j$. This allows us to define arbitrary rank-1 intensity masks and thus selectively apply spilling to specific subsets of sites.

This protocol enables single-shot removal of state $|1\rangle$ atoms without perturbing state $|2\rangle$, providing a flexible method for initializing spin-imbalanced or spatially patterned states. The performance of the method in terms of selectivity and overall fidelity is summarized in Fig. ?. Sequential applications of such steps to prepare arbitrary configurations are discussed in Sec. 4.9.

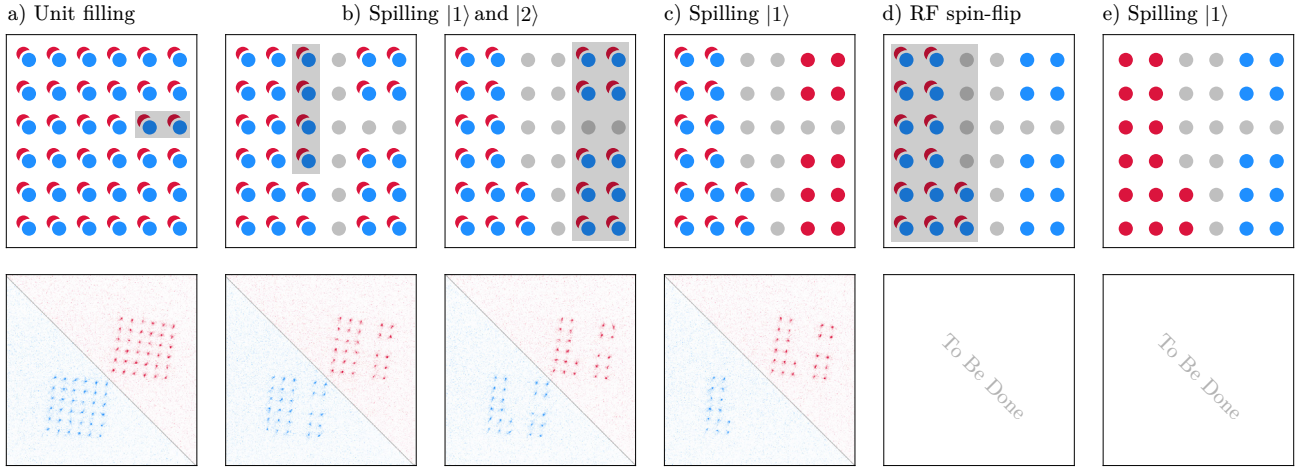


Figure 16: **Sequence for arbitrary filling preparation in a 2D tweezer array.** *Top row:* Schematics of spin- and site-selective atom spilling, with gray shading indicating regions where atoms are removed. Blue and red semicircles represent atoms in different spin states, while gray circles denote emptied sites. *Bottom row:* Experimental snapshots (averaged over 10 realizations) demonstrating each preparation stage. Panels (a)-(c) show completed experimental steps: initial unit filling (a), spilling of both spin states from selected regions (b), and spin-selective spilling of state $|1\rangle$ atoms (c). Panels (d)-(e) illustrate future planned steps, including spin-flip via RF transition (d) and subsequent spilling (e), which have not yet been experimentally realized.

4.9 Arbitrary occupation loading

The ability to prepare arbitrary atom configurations is a key ingredient for bottom-up quantum simulation. After obtaining unit filling for both spin states (as discussed in Sec. 4.5 and 4.8), we implement a multi-stage spilling sequence that enables spin- and site-resolved initialization of arbitrary patterns.

The loading sequence proceeds in several steps:

1. Prepare a $|1\rangle-|2\rangle$ spin mixture with unit filling across the tweezer array.
2. Perform global spilling steps to remove atoms from factorized intensity patterns P_{ij} , affecting both spin states.
3. Apply spin-selective spilling steps to remove atoms in state $|1\rangle$ from additional factorized subsets of sites.
4. Flip the remaining atoms $|1\rangle \leftrightarrow |2\rangle$ using a microwave π -pulse.
5. Repeat spin-selective spilling to further refine the configuration

Factorized removal. Each spilling step removes atoms from sites where the local tweezer depth P_{ij} falls below a certain threshold. Since we can impose any rank-1 intensity mask $P_{ij} = H_i V_j$, it is possible to tailor the removal region to arbitrary product forms. To remove a single atom at site (i', j') , for example, we reduce $H_{i'}$ and $V_{j'}$ by a factor $\eta < 1$ and simultaneously increase the global power by η . This yields a relative intensity of $1/\eta$ at the intersection, while leaving all other sites unchanged or increased in depth. In this way, we can reliably isolate and remove atoms from any desired factorized subset.

Boolean decomposition. We represent the cumulative removal pattern as a binary matrix W_{ij} , where $W_{ij} = 1$ indicates that the atom at site (i, j) has been removed. Each spilling operation adds a binary outer product $u_i^\lambda v_j^\lambda$ via Boolean logic ($1+1=1$). An arbitrary target pattern can therefore be reached through a sequence of such operations:

$$W_{ij} = \bigvee_{\lambda=1}^r u_i^\lambda v_j^\lambda, \quad (15)$$

which defines the exact Boolean matrix factorization (EBMF) of the removal matrix. In the worst case, any binary $n \times n$ matrix admits such a decomposition using at most n steps.

Optimal EBMF. While a naive strategy—such as row- or column-wise removal—may require up to n iterations, we find that optimal EBMF often reduces this number. The problem of finding an exact Boolean matrix factorization with minimal rank is known to be NP-complete [34] and NP-hard to approximate [20]. Nevertheless, for arrays up to 10×10 , optimal decompositions can be computed in a few seconds using a SAT solver. These improvements are particularly useful for minimizing experimental cycle time and improving overall sequence fidelity. A full discussion of the EBMF algorithm and its implementation is presented in Appendix.

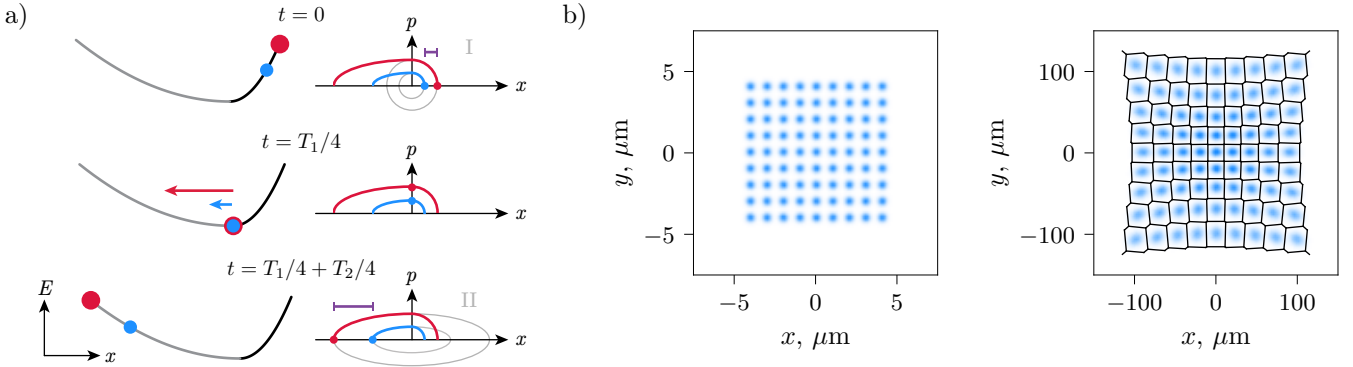


Figure 17: Matter-wave magnification scheme and ROI adaptation. (a) Conceptual illustration of matter-wave magnification: atoms initially localized at the slope of a harmonic potential with frequency ω_1 roll towards the center during a quarter period. Subsequent expansion in a shallower harmonic potential with frequency ω_2 increases their spatial separation by the factor ω_1/ω_2 . (b) Initial atom distribution (left) and magnified pattern after propagation (right), demonstrating distortion due to anharmonicities. Voronoi diagrams adapt the regions of interest (ROI) to these distorted patterns, improving atom detection fidelity.

5 Matter-wave magnifier

5.1 Motivation and overview

Achieving single-site resolution in quantum gas microscopy is crucial for experiments probing quantum many-body phenomena. Conventional imaging techniques typically rely on high numerical aperture (N.A.) objectives to directly resolve atomic distributions in optical lattices. However, even with advanced optics, direct imaging is often limited by the fundamental diffraction limit and the intrinsic diffusion of atoms during photon scattering. In particular, for lattice spacings on the order of a micrometer or below—such as the bow-tie lattice spacing of $0.75\mu\text{m}$ used in our experiment—direct imaging becomes impractical due to both optical resolution limits and momentum kicks received by atoms from resonant imaging light, causing significant spatial diffusion.

To overcome these limitations, we utilize the technique of matter-wave magnification (MWM), which enables significant enlargement of the spatial distribution of atoms prior to the imaging process [26]. MWM operates by carefully engineering the evolution of atomic ensembles through controlled harmonic potentials. This method enlarges spatial patterns coherently, thus facilitating the detection of atomic distributions with improved resolution.

The principle underlying MWM can be understood from the perspective of phase-space dynamics. Consider atoms initially confined near the turning points of a harmonic potential with frequency ω_1 . After evolving for a quarter of the harmonic period $T_1/4 = \pi/2\omega_1$, their spatial distribution transforms entirely into momentum space. Subsequently, atoms are subjected to a second, weaker harmonic potential characterized by frequency ω_2 for another quarter period $T_2/4 = \pi/2\omega_2$. During this second stage, the momentum-space distribution converts back into real space, resulting in magnification by a factor given by the ratio ω_1/ω_2 [26]. From the viewpoint of the Schrödinger equation, each evolution step corresponding to a quarter period in a harmonic potential functions as a Fourier transformation, converting between position and momentum space representations.

However, practical implementation of MWM faces several challenges, notably potential anharmonicities that cause distortions of the magnified atomic pattern. These distortions necessitate adaptive methods for defining regions of interest (ROI) to ensure accurate atom detection. In this work, the application of Voronoi diagrams was introduced to adjust ROI based on actual atomic distributions post-magnification, thus potentially enhancing detection fidelity.

5.2 Numerical modeling

Classical Monte Carlo. To accurately model the classical trajectories of atoms undergoing matter-wave magnification, a numerical Monte Carlo approach combined with the fourth-order Runge-Kutta (RK4) integration method is employed. The RK4 method numerically solves ordinary differential equations with high accuracy, making it ideal for simulating classical dynamics governed by Newtonian mechanics.

The particle trajectories are determined by solving Newton's equations of motion:

$$m \frac{d^2\mathbf{r}}{dt^2} = -\nabla V(\mathbf{r}), \quad (16)$$

where m is the particle mass, and $V(\mathbf{r})$ denotes the potential acting on the atoms. The RK4 algorithm explicitly

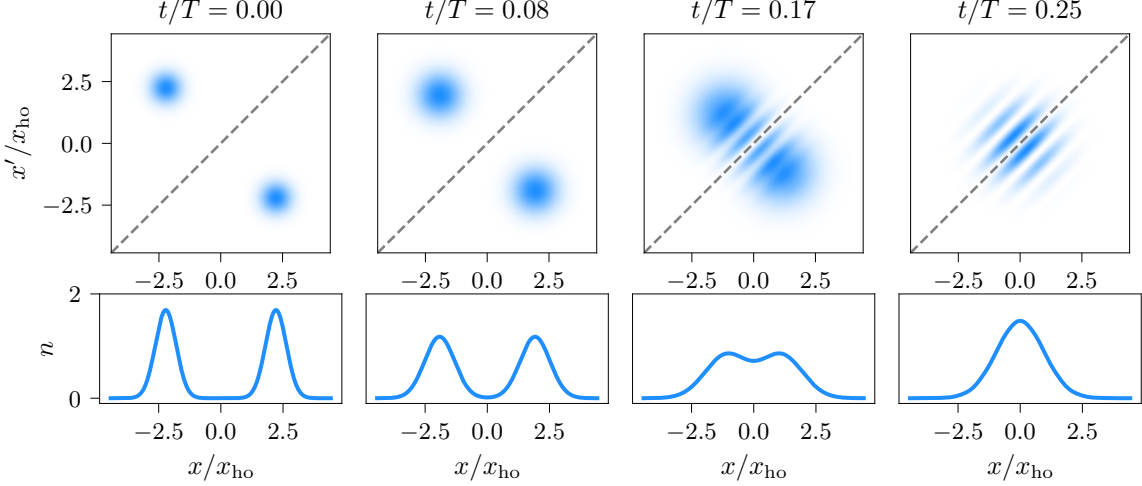


Figure 18: **Two-fermion dynamics in a 1D harmonic trap: quantum statistics.** Top row: Time evolution of the two-particle correlation function $P_2(x, x')$ for two fermions in a harmonic potential. The characteristic anti-bunching dip along the diagonal reflects fermionic quantum statistics, contrasting the bunching peak expected for bosons. Bottom row: Corresponding single-particle density profiles $n(x)$, which remain indistinguishable from the bosonic case, highlighting the necessity of two-particle correlations to probe quantum statistics.

updates positions and momenta at each timestep Δt as follows. Consider a state vector $\mathbf{y}(t) = (\mathbf{r}(t), \mathbf{p}(t))$. Time evolution is determined by:

$$\frac{d\mathbf{y}(t)}{dt} = \mathbf{f}(t, \mathbf{y}(t)), \quad \mathbf{f}(t, \mathbf{y}(t)) = \left(\frac{\mathbf{p}(t)}{m}, -\nabla V(\mathbf{r}(t)) \right).$$

where the right-hand side vector $\mathbf{f}(t, \mathbf{y}(t))$ encapsulates both position and momentum updates.

The RK4 integration method proceeds through intermediate stages:

$$\begin{aligned} \mathbf{k}_1 &= \mathbf{f}(t, \mathbf{y}(t)), \\ \mathbf{k}_2 &= \mathbf{f}\left(t + \frac{1}{2}\Delta t, \mathbf{y}(t) + \frac{1}{2}\mathbf{k}_1\right), \\ \mathbf{k}_3 &= \mathbf{f}\left(t + \frac{1}{2}\Delta t, \mathbf{y}(t) + \frac{1}{2}\mathbf{k}_2\right), \\ \mathbf{k}_4 &= \mathbf{f}\left(t + \Delta t, \mathbf{y}(t) + \mathbf{k}_3\right), \end{aligned}$$

resulting in the updated state vector:

$$\mathbf{y}(t + \Delta t) = \mathbf{y}(t) + \frac{\Delta t}{6} (\mathbf{k}_1 + 2\mathbf{k}_2 + 2\mathbf{k}_3 + \mathbf{k}_4).$$

Initial conditions in Monte Carlo simulations are sampled according to experimentally realistic normal distributions relevant for trapped atoms. The trajectories evolve numerically via the RK4 method with sufficiently small timesteps to ensure numerical precision and stability. GPU acceleration significantly enhances computational performance, allowing the simulation of approximately 1.6×10^6 particles for 1000 RK4 steps in approximately 4 seconds (benchmarking performed on an NVIDIA A100 GPU). In contrast, the same computation performed on a standard CPU (Intel Xeon Gold 6330) typically requires about 100 seconds, highlighting the significant speedup provided by GPU implementation.

The subsequent section describes our quantum mechanical simulations employing the split-step method, which complement the classical approach and address quantum-statistical effects for fermionic atoms.

Split-step method. Complementing the classical Monte Carlo approach, in this work quantum mechanical simulations were employed to capture wavefunction dynamics during matter-wave magnification. Specifically, we utilize the split-step Fourier method, which efficiently solves the time-dependent Schrödinger equation, particularly suitable for systems with spatially varying potentials and wavefunction evolution.

The evolution of the atomic wavefunction $\psi(\mathbf{r}, t)$ is governed by the time-dependent Schrödinger equation:

$$i\hbar \frac{\partial}{\partial t} \psi(\mathbf{r}, t) = \left(-\frac{\hbar^2}{2m} \nabla^2 + V(\mathbf{r}) \right) \psi(\mathbf{r}, t).$$

The split-step method leverages the separation of kinetic and potential energy terms. The propagation over a timestep Δt can be approximated by splitting the evolution operator into kinetic and potential contributions:

$$\psi(\mathbf{r}, t + \Delta t) \approx e^{-i\frac{\Delta t}{2\hbar} V(\mathbf{r})} e^{-i\frac{\Delta t}{\hbar} \frac{\hbar^2}{2m}} e^{-i\frac{\Delta t}{2\hbar} V(\mathbf{r})} \psi(\mathbf{r}, t).$$

The kinetic operator is naturally handled in momentum space via the Fourier transform, as it becomes diagonal:

$$\exp\left(-i\frac{\Delta t}{\hbar}\frac{\hat{p}^2}{2m}\right)\psi(\mathbf{r},t) = \mathcal{F}^{-1}\left[\exp\left(-i\frac{\Delta t}{\hbar}\frac{\hbar^2 k^2}{2m}\right)\mathcal{F}\psi(\mathbf{r},t)\right],$$

where \mathcal{F} denotes the Fourier transform, and k is the momentum-space coordinate. Thus, each evolution step avoids the stringent Courant–Friedrichs–Lewy (CFL) condition encountered in purely spatial methods, allowing for larger and more efficient timesteps.

Quantum treatment via the split-step method becomes particularly relevant when analyzing phenomena sensitive to quantum statistics. While average densities for ensembles of non-interacting atoms can be accurately captured using classical descriptions, quantum approaches are indispensable when studying relative positions of particles within individual realizations—especially for fermions. This is illustrated by considering two fermions in a harmonic trap, where quantum statistics significantly influence the spatial correlation patterns, producing characteristic anti-bunching behavior distinctly observable in the two-particle correlation function $P_2(x,x')$ [5].

Specifically, the fermionic nature imposes Pauli exclusion, manifesting as a pronounced dip in $P_2(x,x')$ along the line $x = x'$, contrasting sharply with the bunching observed in bosonic systems. Such quantum-statistical features, shown explicitly in Fig. 18, are not captured by classical simulations and underscore the necessity of quantum modeling methods like the split-step Fourier approach. Consequently, this technique complements the classical Monte Carlo simulations, providing a numerical framework to support the experimental realization of matter-wave magnification schemes described throughout this work.

The next subsection discusses in detail the Voronoi diagram-based method introduced to adaptively define regions of interest (ROI), mitigating spatial distortions inherent in the magnified atomic distributions.

ROI with Voronoi diagrams. While matter-wave magnification significantly improves the spatial resolution for atomic imaging, practical implementations face challenges arising from anharmonicities and other distortions inherent in realistic trapping potentials. These distortions can lead to irregular spatial distributions, complicating reliable single-atom detection. Consequently, defining appropriate regions of interest (ROI) for each magnified atomic pattern becomes essential to ensure high detection fidelity.

In this work, a robust solution was introduced by employing Voronoi diagrams to adapt the ROI according to the actual spatial distributions observed after magnification. Voronoi diagrams partition a plane into distinct regions based on the distance to a specified set of points, known as "seeds". Each region contains exactly one seed, and any given point within a region is closer to its corresponding seed than to any other seed. Formally, for a set of seed points $\{\mathbf{s}_i\}$, the Voronoi region R_i associated with seed \mathbf{s}_i is defined as:

$$R_i = \mathbf{r} \mid |\mathbf{r} - \mathbf{s}_i| \leq |\mathbf{r} - \mathbf{s}_j|, \quad \forall j \neq i. \quad (17)$$

By using the experimentally determined average final atom positions after the magnification process as seeds, Voronoi diagrams naturally provide adaptive ROIs tailored to distorted atom distributions. This ensures each ROI captures the atom signal associated with its corresponding trap site, even under anharmonic distortion. Voronoi-based ROI allocation minimizes signal contamination between neighboring sites, as each ROI is constructed explicitly to maximize separation from adjacent seed points, thereby reducing overlap.

Within the scope of this thesis, Voronoi diagram-based ROI adaptation was proposed and validated as a method for improving atom detection reliability after MWM. As demonstrated in Fig. 17b, applying Voronoi diagrams enhances detection by systematically accounting for magnification-induced distortions in atomic distributions.

Summary. In this subsection, the concept of matter-wave magnification (MWM) was introduced, a powerful approach to enhance spatial resolution in quantum gas microscopy beyond conventional optical limitations. To accurately describe and optimize the MWM process, two numerical methodologies were implemented. The classical Monte Carlo approach with fourth-order Runge-Kutta (RK4) integration provides efficient simulation of large ensembles of atoms, effectively capturing macroscopic ensemble dynamics. In parallel, the split-step Fourier method addresses quantum-mechanical wavefunction evolution, essential when quantum-statistical effects such as fermionic anti-bunching become relevant. Distortions induced by potential anharmonicities were addressed using Voronoi diagrams. This adaptive method adjusts regions of interest based on observed atomic distributions, ensuring robust atom detection even under realistic experimental conditions.

6 Fermi-Hubbard model: numerical approaches and simulations

6.1 Introduction

Understanding the dynamics of isolated quantum systems remains one of the central goals of contemporary many-body physics. Over the last decades, considerable progress has been made in classifying and probing different dynamical regimes, from thermalizing phases consistent with conventional statistical mechanics to exotic non-ergodic phases that violate the Eigenstate Thermalization Hypothesis (ETH). Among these, the Fermi-Hubbard model has emerged as a paradigmatic platform for studying the interplay of interactions, quantum statistics, and disorder in strongly correlated systems.

In the clean, disorder-free limit, the Fermi-Hubbard model exhibits rich equilibrium physics, including Mott insulators, spin ordering, and pseudogap phenomena relevant to high-temperature superconductivity [17]. However, the model also serves as a fertile ground for exploring nonequilibrium phenomena, such as quantum quenches, relaxation, transport, and entanglement dynamics — especially when generalized to include disorder or spatial inhomogeneities.

Recently, theoretical and experimental attention has increasingly shifted toward the role of disorder in quantum many-body dynamics. It is now understood that disorder can lead to fundamentally different behaviors depending on the presence or absence of interactions. For instance:

- In the absence of interactions, disorder induces *Anderson localization*, which prevents particle diffusion and leads to persistent memory of initial conditions [3].
- When interactions are present, the system may enter the regime of *many-body localization (MBL)*, characterized by the absence of thermalization and slow unbounded entanglement growth [4, 33].
- In contrast, when disorder is weak or absent, the system typically evolves toward local thermal equilibrium, consistent with the predictions of *ETH* [15, 41].

These dynamical phases (*thermal, Anderson-localized, and MBL*) are typically distinguished through the behavior of local observables, spectral statistics, and the dynamics of quantum correlations. Their interplay is especially rich in two dimensions, where the presence of more complex geometry, potential mobility edges, and rare-region effects make the dynamical phase diagram both challenging and intriguing.

From an experimental standpoint, studying such phenomena requires precise control over initial states, evolution Hamiltonians, and high-fidelity measurements of observables at the single-site level. This thesis presents a platform that provides such control, combining deterministic initialization of fermionic states in a two-dimensional tweezer array with programmable evolution under the Fermi-Hubbard Hamiltonian and spin- and site-resolved imaging.

Compared to conventional optical lattice experiments, the tweezer-based approach offers several key advantages for nonequilibrium quantum simulation:

1. *Deterministic and programmable state preparation.* Using a sequence of global and spin-selective spilling operations, arbitrary configurations of fermionic atoms can be prepared with high fidelity. This capability enables initialization of tailored many-body states for probing specific dynamical scenarios, such as local quenches, domain-wall melting, or imbalance relaxation.
2. *Fast experimental cycle and large statistics.* The entire experimental sequence, including preparation, evolution, and measurement, completes in under two seconds, allowing up to 10^5 experimental repetitions per day. This rapid repetition rate is crucial for averaging over disorder realizations and collecting sufficient statistics for dynamical observables.
3. *Spin- and site-resolved detection.* The developed imaging system supports fluorescence-based, single-shot discrimination of atomic spin states on individual lattice sites. This enables direct access to observables such as density profiles $\langle n_j \rangle$, magnetization $\langle \sigma_j^z \rangle$, and spin correlations $\langle \sigma_i^z \sigma_j^z \rangle$ — all of which are sensitive to the system’s dynamical regime.

In tandem with experimental capabilities, in this work a numerical simulation package was developed for modeling real-time dynamics in finite-size Hubbard systems. The package combines exact diagonalization (ED) for small systems and Krylov subspace methods for larger Hilbert spaces (up to 10^9 dimensions), and supports evaluation of observables and entanglement entropy in arbitrary geometries and disorder realizations.

Together, these tools enable a systematic exploration of the dynamical phase diagram of the disordered Fermi-Hubbard model in two dimensions. By leveraging control over initial conditions, disorder strength, and interactions, as well as the ability to access key observables, one can address central questions in nonequilibrium many-body physics:

What determines whether a system thermalizes? When does localization persist in the presence of interactions? How do correlations and entanglement spread in different regimes?

In the following subsections, we review the theoretical framework underpinning these questions, beginning with the concept of thermalization in isolated quantum systems.

6.2 Dynamical phases

Thermalization. A fundamental question in quantum many-body physics concerns how and under which conditions an isolated quantum system approaches thermal equilibrium. Intuitively, thermalization implies that after sufficient evolution time, local observables lose memory of the system's initial conditions and approach steady-state values corresponding to thermodynamic equilibrium [27]. To formalize this concept, consider an isolated quantum system described by a Hamiltonian \hat{H} , evolving from an initial state $|\psi_0\rangle$, which can be expanded in the eigenbasis $|E_j\rangle$ of the Hamiltonian with eigenenergies ε_j as follows:

$$|\psi(t)\rangle = \sum_{j=1}^{\mathcal{N}} c_j e^{-i\varepsilon_j t} |E_j\rangle, \quad (18)$$

where the coefficients are $c_j = \langle E_j | \psi_0 \rangle$, and $\mathcal{N} = \dim \mathcal{H}$ is the dimension of the Hilbert space.

For an arbitrary observable \hat{A} , its expectation value at time t is given by:

$$A(t) = \langle \psi(t) | \hat{A} | \psi(t) \rangle = \sum_{j,k} \bar{c}_k c_j e^{-i(\varepsilon_j - \varepsilon_k)t} \langle E_k | \hat{A} | E_j \rangle. \quad (19)$$

Expanding this further, one separates diagonal and off-diagonal contributions:

$$A(t) = \sum_j |c_j|^2 \langle E_j | \hat{A} | E_j \rangle + \sum_{k \neq j} c_j \bar{c}_k e^{-i(\varepsilon_j - \varepsilon_k)t} \langle E_k | \hat{A} | E_j \rangle. \quad (20)$$

Thermalization at large times, $t \gg t_{\text{th}}$, implies that the observable reaches a steady-state value $A(E)$ with small fluctuations around this average, where $E = \langle \psi_0 | \hat{H} | \psi_0 \rangle$ is the initial energy of the system:

$$A(t \gg t_{\text{th}}) = A(E) + \text{small fluctuations}. \quad (21)$$

Analyzing Eq. (20), the condition for small fluctuations around a steady-state value requires the off-diagonal matrix elements $\langle E_k | \hat{A} | E_j \rangle$, $k \neq j$, to be sufficiently small. Indeed, due to the large number of off-diagonal terms ($\sim \mathcal{N}^2$), their contributions could, in principle, sum up to large fluctuations. To suppress such fluctuations, one typically assumes these off-diagonal matrix elements to be negligible or effectively random, scaling as $1/\sqrt{\mathcal{N}}$.

Furthermore, to ensure that the steady-state expectation value $A(E)$ does not depend sensitively on initial conditions, one additional criterion is necessary: the diagonal elements $\langle E_j | \hat{A} | E_j \rangle$ must vary smoothly with energy:

$$\langle E_j | \hat{A} | E_j \rangle \approx A(\varepsilon_j), \quad (22)$$

where $A(\varepsilon)$ is a continuous and smooth function of energy ε . Under these assumptions, if the initial state $|\psi_0\rangle$ occupies energy eigenstates within a sufficiently narrow energy window ΔE , such that the variation $\partial_E A(E) \Delta E$ is small, we can approximate:

$$A(t \gg t_{\text{th}}) \approx \sum_j |c_j|^2 A(\varepsilon_j) \approx A(E). \quad (23)$$

The conditions described above constitute the Eigenstate Thermalization Hypothesis (ETH), first introduced by Deutsch [15] and later developed by Srednicki [41]. ETH thus posits that individual eigenstates of chaotic quantum many-body systems already encode thermal equilibrium properties, and as long as the system's initial state overlaps with sufficiently many such eigenstates within a narrow energy band, observables will dynamically thermalize at large times.

It is important to note that for isolated quantum systems, the global state remains pure at all times, as indicated by the purity condition $\text{tr}(\rho^2) = 1$. In contrast, a genuinely thermal mixed state would exhibit $\text{tr}(\rho^2) < 1$. Thus, the concept of thermalization in isolated quantum systems pertains specifically to observables rather than the full density matrix. This subtlety motivates the interest in subsystem dynamics: if the total system is partitioned into subsystems Ω_1 and Ω_2 , the reduced density matrix $\rho_1 = \text{tr}_{\Omega_2} \rho$ might indeed become thermal (mixed), while subsystem Ω_2 serves effectively as a thermal bath. This scenario represents a broader context beyond the current discussion but remains an intriguing direction for future experimental and theoretical exploration.

Finally, one should acknowledge the possibility of observable-dependent thermalization. Given the ETH criteria, it is plausible that in certain quantum systems, some observables \hat{A}_1 might thermalize effectively, while others, \hat{A}_2 , may not. Thus, thermalization is not universal, but rather depends on the observable and the particular properties of the quantum system under consideration.

To summarize, thermalization in isolated quantum systems, as described by ETH, occurs when local observables evolve towards stationary, thermal equilibrium values at long times, provided the system's eigenstates satisfy specific criteria regarding their energy dependence and off-diagonal matrix elements.

Anderson localization. Localization phenomena in quantum systems provide striking examples of the breakdown of thermalization and transport, even in the absence of interactions. A fundamental example is Anderson localization, first theoretically described by P. W. Anderson in the seminal work [3], originally in the context of non-interacting electrons in disordered lattices. Anderson localization describes the scenario where the presence of disorder in the potential landscape leads to exponential localization of single-particle wavefunctions and consequently prevents diffusion.

Consider the single-particle Hamiltonian describing hopping of a particle on a lattice with nearest-neighbor tunneling amplitude t and site-dependent random potentials V_i :

$$\hat{H} = -t \sum_{\langle i,j \rangle} (c_i^\dagger c_j + c_j^\dagger c_i) + \sum_i V_i n_i, \quad (24)$$

where c_i^\dagger and c_i are fermionic creation and annihilation operators on lattice site i , and $n_i = c_i^\dagger c_i$ is the number operator. The potentials V_i are typically taken from a random distribution, such as uniformly distributed $V_i \in [-W, W]$, where W characterizes the strength of the disorder.

Anderson demonstrated that in one and two dimensions, any finite amount of disorder is sufficient to localize all eigenstates, rendering them exponentially localized around particular lattice sites. In three-dimensional systems, there exists a critical value of disorder strength, beyond which the system transitions from a metallic (extended) to an insulating (localized) phase [2].

The key consequence of Anderson localization is the absence of diffusion, reflected by the suppression of transport properties and conductivity. A particle initially localized around a particular lattice site remains effectively trapped in a finite spatial region for all times. The wavefunction amplitudes at distant sites decay exponentially:

$$|\psi_j| \sim e^{-|j-j_0|/\xi}, \quad (25)$$

where ξ is known as the localization length, and j_0 is the localization center. Importantly, ξ decreases with increasing disorder strength.

From the perspective of quantum dynamics and thermalization, Anderson-localized systems exhibit fundamentally different behavior compared to systems obeying the Eigenstate Thermalization Hypothesis (ETH). Specifically, observables in Anderson-localized systems typically retain memory of their initial conditions indefinitely, as the system cannot redistribute energy or particle number efficiently. Formally, the off-diagonal matrix elements of observables remain substantial and non-randomized, violating the conditions required by ETH for thermalization.

To illustrate this behavior, consider a single-particle observable, such as the local density at site j , $\hat{n}_j = c_j^\dagger c_j$. Starting from an initially localized wavefunction $|\psi_0\rangle$, the expectation value of the local density at site j evolves as:

$$n_j(t) = \langle \psi(t) | \hat{n}_j | \psi(t) \rangle. \quad (26)$$

For a fully Anderson-localized system, this quantity remains close to its initial value for sites near the initial localization center and does not relax toward a homogeneous distribution, contrasting sharply with the ETH scenario.

It is important to emphasize that Anderson localization relies crucially on the absence of interactions. The presence of even weak interactions between particles can significantly alter the localization properties, either destabilizing localization and restoring ergodicity (thermalization) or giving rise to more complex regimes such as many-body localization (MBL), which will be discussed in the next section.

Experimental investigations of Anderson localization have been successfully realized in various physical platforms, including ultracold atomic gases in disordered or quasiperiodic optical potentials [7, 36]. These experiments confirm the theoretical predictions and demonstrate key signatures such as absence of transport and persistent spatial confinement.

Summarizing, Anderson localization represents a fundamental example of non-thermalizing quantum dynamics, where disorder-induced localization suppresses energy and particle transport. This phenomenon violates the Eigenstate Thermalization Hypothesis, leading to persistent memory effects and long-lived non-equilibrium states, providing a clear contrast to thermalizing quantum systems.

Many-body localization (MBL). While Anderson localization establishes the absence of transport in non-interacting systems due to static disorder, the behavior of *interacting* disordered systems remained an open question for decades. The key insight emerged from the realization that localization can persist even in the presence of interactions, giving rise to the phenomenon of many-body localization (MBL) [4, 33, 1]. MBL represents a genuine breakdown of statistical mechanics in isolated quantum systems: despite having strong interactions and high energy density, such systems do not thermalize and retain long-time memory of their initial conditions.

The MBL regime is most naturally studied in the disordered Fermi-Hubbard model, where the Hamiltonian is:

$$\hat{H} = -t \sum_{\langle i,j \rangle, \sigma} (c_{i\sigma}^\dagger c_{j\sigma} + \text{h.c.}) + U \sum_i n_{i\uparrow} n_{i\downarrow} + \sum_{i,\sigma} V_i n_{i\sigma}. \quad (27)$$

Here, t is the tunneling amplitude, U the on-site interaction strength, and V_i the static disorder potential at site i . The presence of both interactions and disorder sets the stage for competition between delocalization (favored by tunneling and interactions) and localization (favored by disorder). Several observable features distinguish MBL from both Anderson localization and thermalization.

Absence of thermalization. Local observables retain memory of their initial values at arbitrarily long times. For example, if the system is initialized in a charge-density wave state, the imbalance between even and odd sites does not relax to zero:

$$\mathcal{I}(t) = \frac{N_{\text{even}}(t) - N_{\text{odd}}(t)}{N_{\text{even}}(t) + N_{\text{odd}}(t)} \not\rightarrow 0 \quad \text{as } t \rightarrow \infty. \quad (28)$$

Such behavior reflects the failure of the Eigenstate Thermalization Hypothesis (ETH).

Slow entanglement growth. Despite the absence of thermalization, MBL systems can exhibit entanglement growth over time. A hallmark of the MBL phase is a *logarithmic* increase of bipartite entanglement entropy:

$$S(t) \sim \log t, \quad (29)$$

in contrast to linear growth in thermal phases and saturation in Anderson-localized systems. This growth is attributed to dephasing processes mediated by interactions and signals that MBL eigenstates are not strictly product states.

Although both Anderson localization and MBL prevent transport and thermalization, their underlying mechanisms and dynamical signatures differ. Anderson localization arises purely from interference and is static. Entanglement entropy does not grow over time (beyond single-particle effects). MBL is an intrinsically interacting phenomenon. While transport is suppressed, interactions induce dephasing and allow for slow spreading of entanglement and correlations.

These differences manifest in observables such as site-resolved magnetization and entanglement entropy. For instance, in a system initialized with spin imbalance, Anderson localization preserves local magnetization indefinitely, while weak interactions in MBL lead to its decay — even though the system remains non-thermal in terms of density observables. Similarly, growth of subsystem entanglement entropy in MBL (but not in AL) allows clear dynamical distinction.

As disorder strength W is decreased or interaction U is increased, MBL eventually breaks down. Numerical studies identify a sharp transition between MBL and thermalizing phases. However, due to finite-size limitations, precise determination of the transition point remains challenging in two dimensions. Notably, stability of MBL in 2D and higher dimensions has been a subject of debate, with proposed “thermal avalanche” mechanisms [14]. Nevertheless, recent experiments and numerics show robust signatures of MBL-like behavior in 2D systems on experimentally relevant timescales [12, 9, 43].

MBL has been observed in cold atom systems, trapped ions, and superconducting circuits. In particular, ultracold fermionic atoms in disordered optical lattices provide a clean platform for probing MBL [38, 29, 12]. Our experimental platform, offering spin- and site-resolved preparation and readout, is well-suited to systematically study MBL in 2D geometries — including its dynamics, spatial correlations, and response to engineered perturbations.

Integrable limit. An important baseline for understanding quantum thermalization and localization is the behavior of clean, non-interacting systems. In the absence of both interactions and disorder, many-body systems may become integrable — that is, they possess an extensive set of conserved quantities that constrain the dynamics. These systems do not thermalize in the conventional sense, as their dynamics remains quasi-periodic and retains detailed memory of the initial state. This regime provides a sharp contrast to both ETH-obeying thermal systems and disorder-induced localized phases.

Consider the Fermi-Hubbard model with $U = 0$ and $V_i = 0$, i.e., a system of non-interacting fermions hopping on a regular lattice:

$$\hat{H}_0 = -t \sum_{\langle i,j \rangle, \sigma} (c_{i\sigma}^\dagger c_{j\sigma} + \text{h.c.}). \quad (30)$$

This model is diagonalizable in momentum space. The occupation number operators in the single-particle eigenbasis, $\hat{n}_k = c_k^\dagger c_k$, commute with the Hamiltonian and with each other, making them integrals of motion. Consequently, the time evolution of any observable is constrained by the conservation of mode occupations:

$$\frac{d}{dt} \hat{n}_k(t) = 0 \quad \text{for all } k. \quad (31)$$

Such a structure leads to *non-ergodic dynamics*: the system does not explore the full Hilbert space compatible with energy conservation. Instead, its evolution is confined to a restricted subspace determined by the initial conditions. As a result, local observables generally exhibit persistent oscillations or approach non-thermal steady states.

A common illustration is the expansion of a domain-wall initial state, where all fermions are localized on one half of the lattice. In a thermalizing system, this state would relax toward a uniform density. In the integrable limit, however, the density profile exhibits long-lived coherent oscillations, reflecting ballistic propagation of non-interacting wave packets.

While integrable dynamics and many-body localization both lead to non-thermal behavior, they are physically and structurally distinct. Integrable systems lack randomness: the absence of thermalization arises from fine-tuned conservation laws, not disorder. In integrable systems, entanglement entropy typically grows linearly and saturates to a value consistent with GGE; in MBL systems, it grows logarithmically.

In cold atom experiments, the integrable limit is naturally realized by suppressing both interactions (via Feshbach tuning $U \rightarrow 0$) and disorder. This regime serves as a benchmark: any deviation from the predicted integrable dynamics, such as onset of relaxation or loss of coherence, can be attributed to either residual interactions or imperfections. As such, the integrable point provides a valuable reference when exploring more complex dynamical regimes.

The integrable limit of the Fermi-Hubbard model — realized by turning off both disorder and interactions — exhibits non-ergodic, non-thermalizing behavior characterized by coherent dynamics, conserved mode occupations, and failure of ETH. Unlike MBL or Anderson-localized systems, the dynamics is not frozen or spatially confined, but instead evolves in a highly constrained and predictable manner. This regime sets a theoretical and experimental baseline for interpreting deviations due to interactions or disorder.

6.3 Numerical methods

Experimental investigation of quantum many-body dynamics benefits greatly from accurate and scalable numerical modeling. In the context of disordered Fermi-Hubbard systems, such modeling helps in validating measurement protocols and benchmarking physical observables. However, simulating out-of-equilibrium dynamics in two-dimensional systems remains a formidable task due to the exponential growth of the Hilbert space with system size and the rapid entanglement generation in thermalizing regimes.

To address these challenges, a numerical framework was developed in the course of this work. It supports efficient simulation of unitary dynamics in finite two-dimensional Fermi-Hubbard systems with arbitrary geometries, boundary conditions, and disorder realizations. The framework combines two complementary computational strategies:

Exact diagonalization (ED). For systems with Hilbert space dimension up to $\mathcal{N} \sim 10^4$, full diagonalization of the Hamiltonian \hat{H} allows direct computation of all eigenvalues ε_j and eigenstates $|E_j\rangle$. Time evolution of an initial state $|\psi_0\rangle$ is then given by:

$$|\psi(t)\rangle = \sum_j c_j e^{-i\varepsilon_j t} |E_j\rangle, \quad \text{with } c_j = \langle E_j | \psi_0 \rangle. \quad (32)$$

This approach gives access to long-time dynamics, spectral statistics, entanglement entropy, and steady-state observables with machine precision.

Krylov-based time evolution. For larger systems ($\dim \mathcal{H} \sim 10^4\text{--}10^9$), storing the full spectrum becomes infeasible. Instead, the time-evolution operator $e^{-i\hat{H}t}$ is approximated via Krylov subspace projection methods, such as the Lanczos or Arnoldi algorithm [37, 22]. The idea is to construct a Krylov basis $|\psi\rangle, \hat{H}|\psi\rangle, \hat{H}^2|\psi\rangle, \dots$ and evolve the system within this subspace:

$$|\psi(t)\rangle \approx V_m e^{-iH_K t} V_m^\dagger |\psi_0\rangle, \quad (33)$$

where V_m is an orthonormal matrix spanning the Krylov subspace and H_K is the projected Hamiltonian.

The Krylov solver implemented here supports: Fixed particle number sectors, ensuring efficient memory usage by restricting to Hilbert space blocks with specified $(N_\uparrow, N_\downarrow)$; Arbitrary connectivity graphs, allowing modeling of open, periodic, or custom geometries; GPU acceleration, using PyTorch backends to accelerate sparse matrix-vector operations and state evolution on GPUs.

An additional capability developed as part of this numerical toolbox is the estimation of bipartite entanglement entropy during the system's unitary evolution. Given a pure quantum state $|\psi(t)\rangle$, the bipartite entanglement entropy is defined via the reduced density matrix of subsystem A , obtained by tracing out subsystem B :

$$\rho_A = \text{tr}_B |\psi(t)\rangle\langle\psi(t)|, \quad S(\rho_A) = -\text{tr}(\rho_A \log \rho_A). \quad (34)$$

For relatively small systems, it is feasible to explicitly form and diagonalize ρ_A to compute the entropy exactly. However, for larger system sizes explicit storage or diagonalization of the full reduced density matrix becomes computationally prohibitive.

To overcome this challenge, the numerical package employs an efficient randomized Singular Value Decomposition (SVD) algorithm [21] to approximate the singular values of the reshaped wavefunction. Specifically, the full many-body wavefunction $|\psi(t)\rangle$ is represented in a matrix form ψ_{ab} , with indices a and b corresponding to the states of subsystems A and B , respectively. Using randomized SVD, one approximates the leading singular values σ_i of ψ_{ab} ,

Table 1: **Performance benchmarks** (4×4 system, GPU NVIDIA A100). Execution times correspond to Krylov subspace dimension $K = 10$. Columns denote particle numbers N_\uparrow , N_\downarrow , Hilbert-space dimension \mathcal{N} , Hamiltonian construction time T_H , Krylov evolution step time T_{step} , entanglement entropy estimation time via randomized SVD T_{SVD} , and exact diagonalization time T_{ED} .

N_\uparrow	N_\downarrow	\mathcal{N}	T_H	T_{step}	T_{SVD}	T_{ED}
2	2	1.44×10^4	28 ms	8 ms	24 ms	3.5 s
4	4	3.31×10^6	59 ms	33 ms	4.7 s	N/A
8	8	1.66×10^8	110 ms	2.1 s	N/A	N/A

enabling efficient computation of the entanglement entropy:

$$S(\rho_A) = - \sum_i \sigma_i^2 \log(\sigma_i^2). \quad (35)$$

This randomized approach significantly reduces computational overhead and memory requirements, allowing accurate entropy estimation even for large subsystem dimensions. The ability to efficiently track entanglement entropy is particularly valuable when distinguishing dynamical phases: for example, to differentiate Anderson localization (with limited entropy growth) from many-body localization, characterized by persistent logarithmic entropy growth over time.

While MPS-based techniques such as time-evolving block decimation (TEBD) or DMRG-X are widely used for one-dimensional systems, they become less effective in high-dimensional systems or regimes with volume-law entanglement. In thermalizing 2D dynamics, entanglement entropy typically grows too fast for MPS methods to remain efficient. In contrast, Krylov-based methods do not rely on low entanglement and can faithfully simulate early-to-intermediate dynamics regardless of phase.

The developed numerical toolbox allows fast, flexible, and scalable simulation of quantum dynamics in the 2D Fermi-Hubbard model. Combined with the experimental platform, it provides a reliable method for validating nonequilibrium dynamics, extracting key signatures of localization or thermalization, and guiding future measurement protocols.

6.4 Toolbox performance

The numerical toolbox is designed to simulate dynamics governed by the Fermi-Hubbard Hamiltonian on arbitrary lattice geometries. The Hamiltonian considered is generally given by (27). At the core of the implementation is the compact representation of fermionic many-body states using bitwise encoding. Specifically, the occupation number of each lattice site by spin-up and spin-down fermions is stored in two separate binary integers, significantly reducing memory consumption and enhancing computational speed. Each basis state is thus represented as a pair of bit patterns, enabling rapid evaluation of physical operators via bitwise logic. The numbers of spin-up particles, N_\uparrow , and spin-down particles, N_\downarrow , are considered to be conserved.

Performance benchmarks of the numerical toolbox were obtained on a GPU (NVIDIA A100 GPU) for a representative 4×4 lattice system. Benchmark results are summarized in Table 1. For comparison, equivalent calculations performed on a CPU (Intel Xeon Gold 6330) were typically about 40 times slower than those performed on the GPU, underscoring the benefits of GPU acceleration.

These benchmarks demonstrate that the numerical implementation efficiently scales to large Hilbert-space dimensions, facilitating studies of complex quantum dynamics in regimes beyond reach of exact diagonalization approaches. Krylov subspace methods, combined with optimized GPU execution, ensure that simulations remain computationally feasible even for Hilbert-space sizes on the order of 10^8 or greater.

6.5 Simulation example

A key application of the numerical simulation toolbox developed in this work is the systematic exploration and clear identification of dynamical phases in interacting fermionic systems, described by the Fermi-Hubbard Hamiltonian. To illustrate this capability, a concrete numerical experiment is considered here, focusing on distinguishing between three distinct dynamical regimes: thermalization governed by Eigenstate Thermalization Hypothesis (ETH), Anderson localization, and many-body localization (MBL). The main motivation for this numerical investigation is to demonstrate explicitly how carefully chosen initial states and targeted observables facilitate clear experimental signatures distinguishing these different phases.

Initial state and experimental setup. The initial condition selected for this numerical experiment involves a spatially separated arrangement of spin-up and spin-down fermions in a two-dimensional lattice geometry. Specifically,

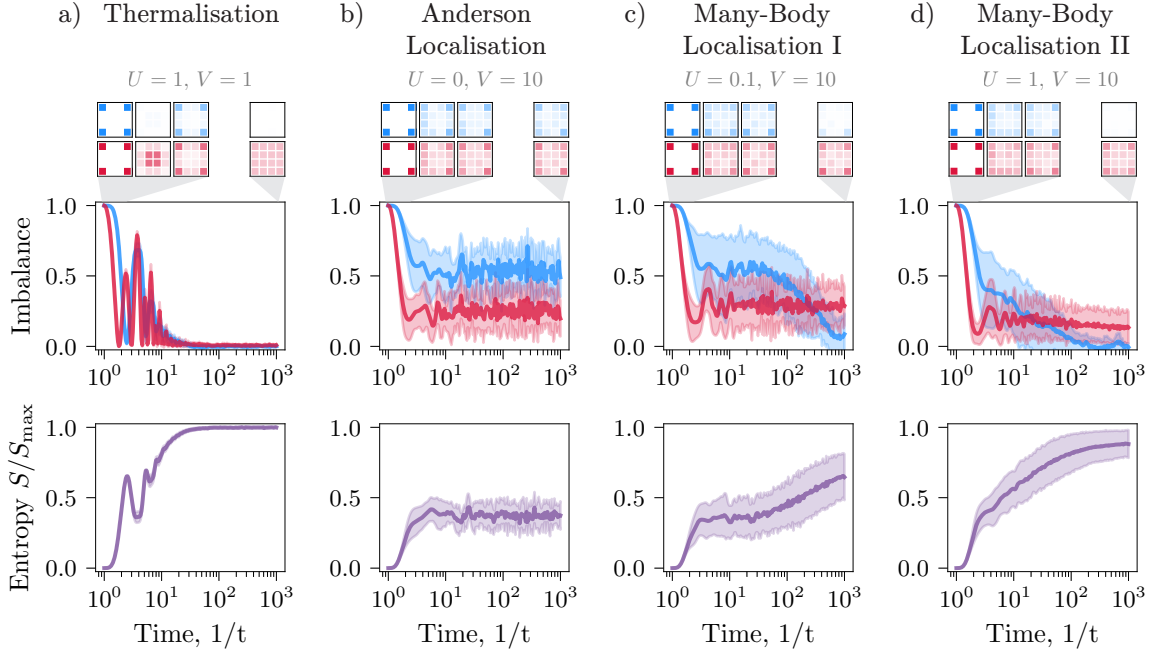


Figure 19: **Dynamical phases in a 2D Fermi-Hubbard system.** *Top:* Snapshots of particle density (red) and magnetization magnitude (blue). *Middle:* Time evolution of density imbalance (red) between corners and bulk, and subsystem magnetization (blue). *Bottom:* Normalized entanglement entropy evolution. All results are averaged over 10 noise realizations; shaded areas indicate standard deviation across realizations. Data were obtained using ED.

the initial wavefunction is prepared with spin-up fermions localized at two diagonally opposite corners of the lattice, and spin-down fermions positioned at the other two corners. This arrangement generates an initial maximal density imbalance between the corners and the lattice bulk, accompanied by a similarly maximal spin imbalance across the system. This choice of initial condition serves two main purposes. First, it creates a strongly non-equilibrium state that provides clear initial reference points for monitoring relaxation dynamics. Second, it allows separate and simultaneous tracking of particle density and spin distribution, thus providing additional insights into the many-body processes at play.

The Hamiltonian parameters considered in this experiment vary across three physically relevant regimes. In particular, the interaction strength U and disorder strength V are systematically tuned to access the thermalization, Anderson localization, and many-body localization regimes. Simulations are performed using exact diagonalization. For reliable statistics, the results reported in this numerical experiment are averaged over ten independent disorder realizations.

Observables and their physical significance. Three primary observables are investigated in this numerical experiment to characterize and distinguish among the dynamical phases mentioned above. The first observable is the particle density imbalance, defined as the normalized difference between particle densities at initially occupied corner sites and the bulk sites. Formally, this imbalance can be expressed as

$$\mathcal{I}(t) = \frac{N_{\text{corner}}(t) - N_{\text{bulk}}(t)}{N_{\text{corner}}(t) + N_{\text{bulk}}(t)}, \quad (36)$$

where $N_{\text{corner}}(t)$ and $N_{\text{bulk}}(t)$ represent particle numbers at corner and bulk sites, respectively, at time t . This observable is sensitive to particle redistribution across the lattice, clearly distinguishing thermalization (complete imbalance relaxation), Anderson localization (persistent imbalance), and intermediate behavior in MBL.

The second observable investigated is the subsystem magnetization $\langle \sigma_j^z \rangle$, representing local spin polarization at individual lattice sites. Unlike particle density imbalance alone, magnetization provides further crucial differentiation between Anderson localization, where spin distributions remain essentially static due to absence of interactions, and MBL or thermalization regimes, where spins dynamically rearrange due to interactions.

The third observable employed is the bipartite entanglement entropy, defined by partitioning the lattice system into two equal subsystems. This entropy provides direct insight into the correlation dynamics and quantum information propagation in the system, with characteristic signatures distinctly differentiating ETH, Anderson localization, and MBL phases.

The numerical results of this illustrative experiment are summarized in Fig. 19. These simulations clearly demon-

strate distinct behavior across different regimes, highlighting the utility of the numerical toolbox in characterizing these dynamical phases.

Thermalization regime (ETH). For parameters corresponding to moderate interaction strength and weak disorder ($U = 1$, $V = 1$), the numerical results show rapid and complete relaxation of the particle density imbalance to zero, indicating full particle redistribution throughout the lattice. Simultaneously, the subsystem magnetization vanishes on similarly short timescales, clearly reflecting efficient spin mixing driven by interactions. The entanglement entropy exhibits rapid initial growth, quickly reaching saturation at values approaching maximal entropy for the subsystem. These dynamical signatures precisely match theoretical predictions from the ETH framework, wherein local observables lose memory of initial conditions and approach thermodynamic equilibrium at late times [15, 41].

Anderson localization regime. In contrast, the numerical simulations at zero interaction and strong disorder strength ($U = 0$, $V = 10$) demonstrate distinct dynamical signatures characteristic of Anderson localization. The particle density imbalance remains nearly constant throughout the time evolution, showing negligible redistribution of particles from initial localized positions. Furthermore, subsystem magnetization remains stable, indicating minimal spin rearrangements. Crucially, the entanglement entropy shows almost no growth, stabilizing at values near zero, indicative of the absence of significant entanglement generation. These results clearly align with the theoretical expectation of Anderson localization, where the absence of interactions ensures persistence of initial conditions indefinitely [3, 2].

Many-body localization regime. For finite interactions in a strongly disordered environment ($U = 0.1$ or $U = 1$, with $V = 10$), the numerical simulations show the hallmark features of many-body localization. In this regime, the particle imbalance partially relaxes but stabilizes at a finite nonzero value, signifying the suppression but not complete absence of transport. In sharp contrast to Anderson localization, the subsystem magnetization gradually diminishes over time, reflecting slow spin thermalization due to interactions, despite the presence of disorder. Most importantly, the entanglement entropy in this regime exhibits a slow, logarithmic increase without saturating quickly, distinguishing MBL from the other phases clearly. This slow entanglement growth is a distinct theoretical signature of MBL and arises fundamentally from interactions and dephasing processes absent in non-interacting localization scenarios [4, 33].

Experimental relevance and further perspectives. The presented numerical results illustrate the feasibility of using carefully designed initial states and targeted observables to experimentally distinguish among ETH, Anderson localization, and MBL phases. In particular, simultaneous measurements of particle density, spin magnetization, and entanglement entropy can be directly implemented in experimental setups such as quantum gas microscopes or tweezer arrays, as discussed in previous sections.

Numerical simulations predict characteristic timescales and clear observable signatures for each dynamical phase, providing concrete guidelines for experimental protocols. Furthermore, recently developed experimental methods for measuring entanglement entropy, such as randomized unitaries, offer realistic pathways for direct verification of theoretical predictions.

7 Appendix

7.1 Boolean matrix factorization

Context and Motivation. In the context of this experimental work, deterministic preparation of atomic patterns in optical tweezer arrays is realized through sequential spilling operations, enabled by a simplified optical setup based exclusively on two orthogonal acousto-optic deflectors (AOD). Unlike more complex approaches employing spatial light modulators (SLM) or digital micromirror devices (DMD), the AOD-based setup restricts the accessible intensity patterns to products of one-dimensional horizontal and vertical profiles:

$$P_{ij} = H_i V_j.$$

Within this scheme, the removal of atoms from selected lattice sites is achieved by appropriately reducing the local tweezer intensities below a tunneling threshold, causing controlled spilling of atoms from targeted sites. Each spilling operation thus imposes a binary removal mask, which, due to the rank-1 intensity structure, factorizes into an outer product of binary vectors $u_i v_j$ where $u_i v_j = 1$ corresponds to a removed atom at site (i, j) .

For general state preparation tasks requiring removal patterns of higher complexity, multiple spilling steps must be applied sequentially. The cumulative removal pattern, obtained after r sequential spilling operations, corresponds to a Boolean sum of rank-1 outer products:

$$W_{ij} = \bigvee_{\lambda=1}^r u_i^\lambda v_j^\lambda,$$

with the logical OR performed element-wise. This equation defines the Exact Boolean Matrix Factorization (EBMF) of the target removal pattern W , and r corresponds to its Boolean rank.

A straightforward method to achieve any target pattern would involve sequential removal operations addressing individual rows or columns independently. Such an approach guarantees factorization for an $n \times n$ matrix in at most n spilling steps. However, this naive strategy typically results in redundant steps and thus slightly extends experimental cycle times and decrease overall fidelities.

Optimal BMF as SAT. Finding the exact Boolean matrix factorization (EBMF) with minimal Boolean rank is a challenging computational task, known to be NP-complete[34] and NP-hard to approximate[20]. Consequently, exact solutions are generally computationally feasible only for relatively small-scale matrices. Within the scope of this thesis, an approach for obtaining optimal EBMF solutions was developed by formulating the problem as a Boolean satisfiability (SAT) task. A SAT problem involves determining whether a set of Boolean variables can satisfy a given logical expression represented in conjunctive normal form (CNF), defined as a conjunction of disjunctions (clauses).

To cast the EBMF into a SAT framework, consider a binary target matrix $M \in \{0, 1\}^{n \times n}$ that we aim to factorize into Boolean matrices $H \in \{0, 1\}^{n \times r}$ and $W \in \{0, 1\}^{r \times n}$ such that:

$$M_{ij} = \bigvee_{k=1}^r H_{ik} W_{kj}.$$

Introducing auxiliary Boolean variables $Z_{ijk} = H_{ik} \wedge W_{kj}$, the above relation can be equivalently expressed as:

$$M_{ij} = \bigvee_{k=1}^r Z_{ijk}. \quad (37)$$

Each auxiliary variable Z_{ijk} is constrained by the logical equivalence:

$$Z_{ijk} \leftrightarrow (H_{ik} \wedge W_{kj}),$$

which, when converted into CNF clauses, yields:

$$\begin{aligned} Z_{ijk} \rightarrow H_{ik} : & \quad (\neg Z_{ijk} \vee H_{ik}) \\ Z_{ijk} \rightarrow W_{kj} : & \quad (\neg Z_{ijk} \vee W_{kj}) \\ H_{ik} \wedge W_{kj} \rightarrow Z_{ijk} : & \quad (\neg H_{ik} \vee \neg W_{kj} \vee Z_{ijk}). \end{aligned}$$

Additionally, the entries of the target matrix M impose further constraints. For every entry $M_{ij} = 1$, at least one corresponding variable Z_{ijk} must be true:

$$(Z_{ij1} \vee Z_{ij2} \vee \dots \vee Z_{ijr}),$$

while for every $M_{ij} = 0$, all corresponding variables must be false:

$$\bigwedge_{k=1}^r (\neg Z_{ijk}).$$

This logical framework fully encodes the Boolean factorization into a CNF formula suitable for modern SAT solvers. Using this SAT-based formulation, the minimal Boolean rank r for a given matrix M can be efficiently found through

Table 2: SAT-based EBMF performance. Computation times and average number of required spilling steps as a function of array size.

Array size	Computation time	Avg. spilling steps
4×4	0.6 ms	3.1
6×6	3.7 ms	4.9
8×8	60 ms	6.7
9×9	0.31 s	7.7

iterative solution attempts, incrementally testing higher values of r until the minimal factorization is obtained.

In practice, employing a SAT solver (such as PycoSAT) proved efficient and reliable for arrays up to approximately 10×10 . This approach, developed and implemented in this thesis, enables optimal experimental sequences for atomic removal.

Performance. To solve the formulated Boolean satisfiability (SAT) problem corresponding to the optimal Boolean matrix factorization, the PycoSAT solver was employed. The workflow consists of translating the EBMF task into conjunctive normal form (CNF) and incrementally increasing the candidate rank r until the solver identifies a valid factorization. The minimal rank r obtained through this procedure directly defines the minimal number of spilling steps required experimentally.

The computational efficiency and experimental impact of this SAT-based approach were systematically characterized by solving randomly generated binary matrices of varying dimensions. Typical solver runtimes and corresponding average number of spilling steps are summarized in Table 2. This analysis demonstrates that optimal EBMF sequences can be computed rapidly and reliably for arrays up to approximately 9×9 . At the larger size of 10×10 , the computational increases, resulting in solver failures in approximately 20% of cases; hence, results for this size are not presented here. Nevertheless, within the experimentally relevant array dimensions, the developed SAT-based approach consistently reduces the required spilling steps.

7.2 Determinantal Point Processes

A central challenge in quantum many-body systems involving indistinguishable fermionic particles is the accurate modeling of the fermionic antisymmetry in the many-body wavefunction. Even in the case of non-interacting fermions, the generation of realistic samples of experimentally observable quantities—such as single-shot atomic density measurements—requires proper antisymmetrization. As the number of particles and the dimensionality of the system increase, enforcing these antisymmetric constraints becomes computationally demanding. For example, treating antisymmetric wavefunctions explicitly for as few as four fermions in two dimensions already presents nontrivial computational difficulties.

To mitigate this challenge, Determinantal Point Processes (DPPs) are employed as a probabilistic framework inherently suited to capturing fermionic statistics. DPPs naturally model repulsive correlations between particles, reflecting the Pauli exclusion principle, and provide a mathematically principled and computationally efficient approach for sampling particle configurations from single-particle wavefunctions.

In experiments reporting the observation of "Pauli crystals"—ordered spatial structures emerging solely from quantum statistical effects—analytical sampling expressions have been derived under restrictive symmetry assumptions. However, in broader experimental contexts, such analytical forms are typically unavailable. In these cases, the DPP-based approach offers a general-purpose numerical method for simulating atomic distributions across diverse trapping geometries.

The following sections present a formal mathematical description of Determinantal Point Processes, detail the algorithmic procedures for DPP sampling, and compare the computational efficiency with that of direct antisymmetrization. The method's practical utility is illustrated through numerical examples, including the reproduction of characteristic correlation features (see Fig.18) using DPP-based simulations (see Fig.20).

Mathematical formulation. Formally, a Determinantal Point Process on a space Λ equipped with a suitable reference measure μ is defined through a kernel function $K(x, y)$, where $x, y \in \Lambda$. For a DPP, the probability of observing a configuration of points $\{x_1, x_2, \dots, x_n\}$ is proportional to the determinant of a corresponding kernel matrix formed by evaluating K at these points:

$$P(x_1, x_2, \dots, x_n) \propto \det[K(x_i, x_j)]_{1 \leq i, j \leq n}. \quad (38)$$

This determinantal structure naturally encodes repulsive correlations between points, making DPPs particularly well-suited for modeling fermionic systems where identical particles exhibit antisymmetric quantum statistics. Specifically,

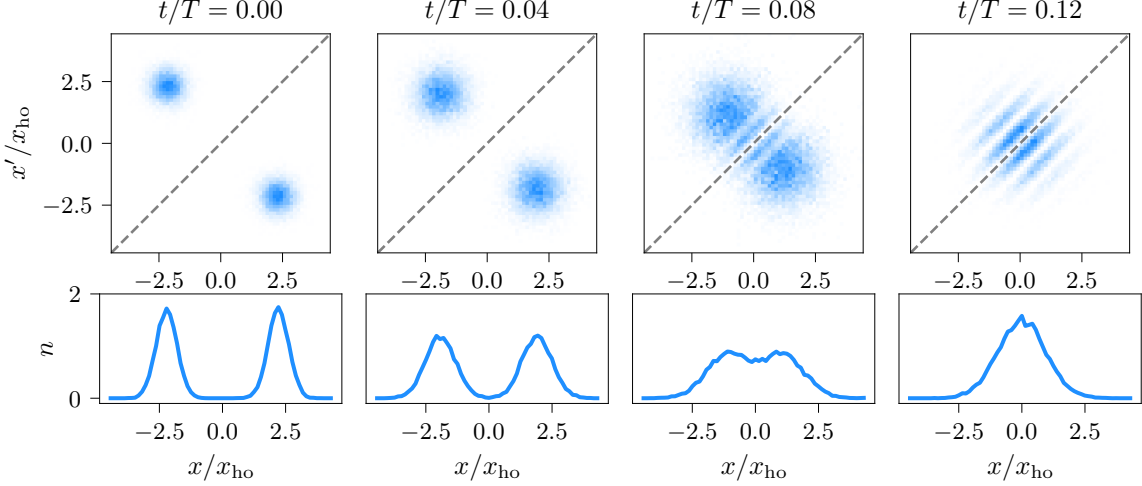


Figure 20: DPP based

the kernel $K(x, y)$ typically corresponds to the two-point correlation function derived from the underlying single-particle wavefunctions:

$$K(x, y) = \sum_k \lambda_k \phi_k(x) \phi_k^*(y), \quad (39)$$

where $\{\phi_k\}$ form an orthonormal set of eigenfunctions of a corresponding integral operator, and $\{\lambda_k\}$ are the associated eigenvalues, bounded between 0 and 1 to guarantee the existence of the process [25].

The fundamental advantage of DPPs lies in their efficient sampling procedure, which bypasses the combinatorial complexity of directly antisymmetrizing wavefunctions. Specifically, if the kernel represents a projection operator (i.e., λ_k equals either 0 or 1), the DPP simplifies to a projection DPP, significantly enhancing computational tractability.

Given a projection kernel K , the sampling procedure of a projection DPP begins by computing the eigen-decomposition of the kernel K :

$$K(x, y) = \sum_{k=1}^M \phi_k(x) \phi_k^*(y), \quad (40)$$

where $\{\phi_k\}$ form an orthonormal basis of the subspace associated with eigenvalue 1. The algorithm then initializes an empty set Y and proceeds iteratively. At each iteration, selection probabilities are computed proportional to:

$$p(x) = \frac{1}{M} \sum_{k=1}^M |\phi_k(x)|^2. \quad (41)$$

A point x is selected according to $p(x)$, after which the subspace is updated by projecting out the selected function:

$$\phi_k(x) \rightarrow \phi_k(x) - \sum_j \frac{\phi_j(x_{\text{selected}})}{\phi_j(x)} \phi_k(x_{\text{selected}}), \quad (42)$$

and the resulting basis set is renormalized. The selected point is added to Y , M is decreased, and the process repeats until $M = 0$. This approach efficiently generates sample realizations that adhere to the correct fermionic antisymmetry without explicitly antisymmetrizing wavefunctions.

Direct antisymmetrization of wavefunctions involves computing determinants of large matrices for every possible configuration, resulting in computational complexity that scales factorially with the particle number. In contrast, the projection-DPP sampling method described above significantly reduces complexity. It scales polynomially in both the number of points sampled and the number of eigenfunctions, typically providing practical feasibility for experimental scenarios involving tens or hundreds of particles.

Nevertheless, obtaining the eigen-decomposition of the kernel can become computationally intensive for large continuous spaces. Therefore, numerical implementations typically utilize efficient algorithms and GPU acceleration to handle realistic experimental scales, as demonstrated earlier in this thesis.

In the following section, we illustrate the application of this DPP sampling approach by replicating the quantum correlation results previously shown in Fig. 18, demonstrating how realistic experimental snapshots can be efficiently generated using Determinantal Point Processes (Fig. 20).

References

- [1] Dmitry A. Abanin, Ehud Altman, Immanuel Bloch, and Maksym Serbyn. Colloquium: Many-body localization, thermalization, and entanglement. *Reviews of Modern Physics*, 91(2):021001, May 2019.
- [2] Elihu Abrahams. *50 years of Anderson localization*. World Scientific Pub. Co, Singapore Hackensack, N.J, 2010.
- [3] P. W. Anderson. Absence of Diffusion in Certain Random Lattices. *Physical Review*, 109(5):1492–1505, March 1958.
- [4] D. M. Basko, I. L. Aleiner, and B. L. Altshuler. Metal–insulator transition in a weakly interacting many-electron system with localized single-particle states. *Annals of Physics*, 321(5):1126–1205, May 2006.
- [5] Andrea Bergschneider, Vincent M. Klinkhamer, Jan Hendrik Becher, Ralf Klemt, Lukas Palm, Gerhard Zürn, Selim Jochim, and Philipp M. Preiss. Experimental Characterization of Two-Particle Entanglement through Position and Momentum Correlations. *Nature Physics*, 15(7):640–644, July 2019.
- [6] Andrea Bergschneider, Vincent M. Klinkhamer, Jan Hendrik Becher, Ralf Klemt, Gerhard Zürn, Philipp M. Preiss, and Selim Jochim. Spin-resolved single-atom imaging of ${}^6\text{Li}$ in free space. *Physical Review A*, 97(6):063613, June 2018.
- [7] Juliette Billy, Vincent Josse, Zhanchun Zuo, Alain Bernard, Ben Hambrecht, Pierre Lugan, David Clément, Laurent Sanchez-Palencia, Philippe Bouyer, and Alain Aspect. Direct observation of Anderson localization of matter waves in a controlled disorder. *Nature*, 453(7197):891–894, June 2008.
- [8] Martin Boll, Timon A. Hilker, Guillaume Salomon, Ahmed Omran, Jacopo Nespolo, Lode Pollet, Immanuel Bloch, and Christian Gross. Spin- and density-resolved microscopy of antiferromagnetic correlations in Fermi-Hubbard chains. *Science*, 353(6305):1257–1260, September 2016.
- [9] Pranjali Bordia, Henrik Lüschen, Sebastian Scherg, Sarang Gopalakrishnan, Michael Knap, Ulrich Schneider, and Immanuel Bloch. Probing Slow Relaxation and Many-Body Localization in Two-Dimensional Quasiperiodic Systems. *Physical Review X*, 7(4):041047, November 2017.
- [10] Antoine Browaeys and Thierry Lahaye. Many-body physics with individually controlled Rydberg atoms. *Nature Physics*, 16(2):132–142, February 2020.
- [11] Tiff Brydges, Andreas Elben, Petar Jurcevic, Benoît Vermersch, Christine Maier, Ben P. Lanyon, Peter Zoller, Rainer Blatt, and Christian F. Roos. Probing Rényi entanglement entropy via randomized measurements. *Science*, 364(6437):260–263, April 2019.
- [12] Jae-yoon Choi, Sebastian Hild, Johannes Zeiher, Peter Schauß, Antonio Rubio-Abadal, Tarik Yefsah, Vedika Khemani, David A. Huse, Immanuel Bloch, and Christian Gross. Exploring the many-body localization transition in two dimensions. *Science*, 352(6293):1547–1552, June 2016.
- [13] Marcus Culemann. *Construction and Control of a Dark Spot Optical Tweezer Array for a Quantum Gas Microscope*. Master’s thesis, Ludwig-Maximilians-Universität München, Munich, 2024.
- [14] Wojciech De Roeck and François Huveneers. Stability and instability towards delocalization in many-body localization systems. *Physical Review B*, 95(15):155129, April 2017.
- [15] J. M. Deutsch. Quantum statistical mechanics in a closed system. *Physical Review A*, 43(4):2046–2049, February 1991.
- [16] Daniel Noah Dux. *An Optical Lattice with Tunable Geometry for a new Fermi-Hubbard Simulator*. PhD thesis, 2023.
- [17] Tilman Esslinger. Fermi-Hubbard Physics with Atoms in an Optical Lattice. *Annual Review of Condensed Matter Physics*, 1(Volume 1, 2010):129–152, August 2010.
- [18] Michael Eric Gehm. *Preparation of an optically-trapped degenerate Fermi gas of ${}^6\text{Li}$: Finding the route to degeneracy*. PhD thesis, January 2003.
- [19] Christian Gross and Immanuel Bloch. Quantum simulations with ultracold atoms in optical lattices. *Science*, 357(6355):995–1001, September 2017.

- [20] Hermann Gruber and Markus Holzer. Inapproximability of Nondeterministic State and Transition Complexity Assuming P \neq NP. In *Developments in Language Theory*, pages 205–216, Berlin, Heidelberg, 2007. Springer.
- [21] N. Halko, P. G. Martinsson, and J. A. Tropp. Finding Structure with Randomness: Probabilistic Algorithms for Constructing Approximate Matrix Decompositions. *SIAM Review*, 53(2):217–288, January 2011.
- [22] Marlis Hochbruck and Christian Lubich. On Krylov Subspace Approximations to the Matrix Exponential Operator. *SIAM Journal on Numerical Analysis*, 34(5):1911–1925, 1997.
- [23] Marvin Holten. *From Pauli Blocking to Cooper Pairs: Emergence in a Mesoscopic 2D Fermi Gas*. PhD thesis, 2022.
- [24] Marvin Holten, Luca Bayha, Keerthan Subramanian, Carl Heintze, Philipp M. Preiss, and Selim Jochim. Observation of Pauli Crystals. *Physical Review Letters*, 126(2):020401, January 2021.
- [25] J. Ben Hough, Manjunath Krishnapur, Yuval Peres, and Bálint Virág. Determinantal Processes and Independence. *Probability Surveys*, 3(none), January 2006.
- [26] Xinyi Huang. *Construction of an Optical Accordion Lattice for a Fermionic Quantum Gas Microscope*. Master’s thesis, 2024.
- [27] Sergei Khlebnikov and Martin Kruczenski. Thermalization of isolated quantum systems, March 2014.
- [28] Joannis Koepsell. *Quantum simulation of doped two-dimensional Mott insulators*. PhD thesis, 2021.
- [29] S. S. Kondov, W. R. McGehee, W. Xu, and B. DeMarco. Disorder-induced Localization in a Strongly Correlated Atomic Hubbard Gas. *Physical Review Letters*, 114(8):083002, February 2015.
- [30] Jonas Kruip. *Design and Assembly of a Microscope Setup for Ultracold Lithium Atoms*. PhD thesis, 2024.
- [31] Alex Kulesza and Ben Taskar. Determinantal point processes for machine learning. *Foundations and Trends® in Machine Learning*, 5(2-3):123–286, 2012.
- [32] Lev Landau. Zur Theorie der Energieübertragung. II. *Physikalische Zeitschrift der Sowjetunion*, 2:46–51, 1932.
- [33] Rahul Nandkishore and David A. Huse. Many-Body Localization and Thermalization in Quantum Statistical Mechanics. *Annual Review of Condensed Matter Physics*, 6(Volume 6, 2015):15–38, March 2015.
- [34] James Orlin. Contentment in graph theory: Covering graphs with cliques. *Indagationes Mathematicae (Proceedings)*, 80(5):406–424, January 1977.
- [35] Maxwell F. Parsons, Anton Maziurenko, Christie S. Chiu, Geoffrey Ji, Daniel Greif, and Markus Greiner. Site-resolved measurement of the spin-correlation function in the Fermi-Hubbard model. *Science*, 353(6305):1253–1256, September 2016.
- [36] Giacomo Roati, Chiara D’Errico, Leonardo Fallani, Marco Fattori, Chiara Fort, Matteo Zaccanti, Giovanni Modugno, Michele Modugno, and Massimo Inguscio. Anderson localization of a non-interacting Bose-Einstein condensate. *Nature*, 453(7197):895–898, June 2008.
- [37] Y. Saad. Analysis of Some Krylov Subspace Approximations to the Matrix Exponential Operator. *SIAM Journal on Numerical Analysis*, 29(1):209–228, 1992.
- [38] Michael Schreiber, Sean S. Hodgman, Pranjal Bordia, Henrik P. Lüschen, Mark H. Fischer, Ronen Vosk, Ehud Altman, Ulrich Schneider, and Immanuel Bloch. Observation of many-body localization of interacting fermions in a quasirandom optical lattice. *Science*, 349(6250):842–845, August 2015.
- [39] Friedhelm Serwane. *Deterministic preparation of a tunable few-fermion system*. PhD thesis, 2011.
- [40] Benjamin M. Spar, Elmer Guardado-Sánchez, Sungjae Chi, Zoe Z. Yan, and Waseem S. Bakr. Realization of a Fermi-Hubbard Optical Tweezer Array. *Physical Review Letters*, 128(22):223202, June 2022.
- [41] Mark Srednicki. Chaos and quantum thermalization. *Physical Review E*, 50(2):888–901, August 1994.
- [42] Lin Su, Alexander Douglas, Michal Szurek, Anne H. Hébert, Aaron Krahn, Robin Groth, Gregory A. Phelps, Ognjen Marković, and Markus Greiner. Fast single atom imaging for optical lattice arrays. *Nature Communications*, 16(1):1017, January 2025.

- [43] Thorsten B. Wahl, Arijeet Pal, and Steven H. Simon. Signatures of the Many-body Localized Regime in Two Dimensions. *Nature Physics*, 15(2):164–169, February 2019.
- [44] Zoe Z. Yan, Benjamin M. Spar, Max L. Prichard, Sungjae Chi, Hao-Tian Wei, Eduardo Ibarra-García-Padilla, Kaden R.A. Hazzard, and Waseem S. Bakr. Two-Dimensional Programmable Tweezer Arrays of Fermions. *Physical Review Letters*, 129(12):123201, September 2022.
- [45] Clarence Zener and Ralph Howard Fowler. Non-adiabatic crossing of energy levels. *Proceedings of the Royal Society of London. Series A, Containing Papers of a Mathematical and Physical Character*, 137(833):696–702, January 1997.
- [46] Gerhard Zürn. *Few-fermion systems in one dimension*. PhD thesis, 2012.
- [47] N. Šibalić, J. D. Pritchard, C. S. Adams, and K. J. Weatherill. ARC: An open-source library for calculating properties of alkali Rydberg atoms. *Computer Physics Communications*, 220:319–331, November 2017.